

# Response Uniformity of the ATLAS Liquid Argon Electromagnetic Calorimeter

M. Aharrouche<sup>a,4</sup>, J. Colas<sup>a</sup>, L. Di Ciaccio<sup>a</sup>, M. El Kacimi<sup>a,4</sup>,  
 O. Gaumer<sup>a,1</sup>, M. Gouanère<sup>a</sup>, D. Goujdami<sup>a,4</sup>, R. Lafaye<sup>a</sup>,  
 S. Laplace<sup>a</sup>, C. Le Maner<sup>a,3</sup>, L. Neukermans<sup>a,11</sup>, P. Perrodo<sup>a</sup>,  
 L. Poggioli<sup>a,9</sup>, D. Prieur<sup>a,2</sup>, H. Przysiezniak<sup>a</sup>, G. Sauvage<sup>a</sup>,  
 I. Wingerter-Seez<sup>a</sup>, R. Zitoun<sup>a</sup>, F. Lanni<sup>b</sup>, L. Lu<sup>b</sup>, H. Ma<sup>b</sup>,  
 S. Rajagopalan<sup>b</sup>, H. Takai<sup>b</sup>, A. Belymam<sup>c</sup>, D. Benchekroun<sup>c</sup>,  
 M. Hakimi<sup>c</sup>, A. Hoummada<sup>c</sup>, Y. Gao<sup>d</sup>, R. Stroynowski<sup>d</sup>,  
 M. Alekса<sup>e</sup>, T. Carli<sup>e</sup>, P. Fassnacht<sup>e</sup>, F. Gianotti<sup>e</sup>, L. Hervas<sup>e</sup>,  
 W. Lampl<sup>e</sup>, J. Collot<sup>f</sup>, J.Y. Hostachy<sup>f</sup>, F. Ledroit-Guillon<sup>f</sup>,  
 F. Malek<sup>f</sup>, P. Martin<sup>f</sup>, S. Viret<sup>f</sup>, M. Leltchouk<sup>g</sup>,  
 J.A. Parsons<sup>g</sup>, S. Simion<sup>g</sup>, F. Barreiro<sup>h</sup>, J. Del Peso<sup>h</sup>,  
 L. Labarga<sup>h</sup>, C. Oliver<sup>h</sup>, S. Rodier<sup>h</sup>, P. Barrillon<sup>i,9</sup>,  
 C. Benchouk<sup>i,10</sup>, F. Djama<sup>i</sup>, F. Hubaut<sup>i</sup>, E. Monnier<sup>i</sup>,  
 P. Pralavorio<sup>i</sup>, D. Sauvage<sup>i,5</sup>, C. Serfon<sup>i</sup>, S. Tisserant<sup>i</sup>,  
 J. Toth<sup>i,6</sup>, D. Banfi<sup>j</sup>, L. Carminati<sup>j</sup>, D. Cavalli<sup>j</sup>, G. Costa<sup>j</sup>,  
 M. Delmastro<sup>j</sup>, M. Fanti<sup>j</sup>, L. Mandelli<sup>j</sup>, M. Mazzanti<sup>j</sup>,  
 G. F. Tartarelli<sup>j</sup>, K. Kotov<sup>k</sup>, A. Maslennikov<sup>k</sup>, G. Pospelov<sup>k</sup>,  
 Yu. Tikhonov<sup>k</sup>, C. Bourdarios<sup>l</sup>, L. Fayard<sup>l</sup>, D. Fournier<sup>l</sup>,  
 L. Iconomidou-Fayard<sup>l</sup>, M. Kado<sup>l,7</sup>, G. Parrou<sup>l</sup>, P. Puzo<sup>l</sup>,  
 D. Rousseau<sup>l</sup>, R. Sacco<sup>l,8</sup>, L. Serin<sup>l</sup>, G. Unal<sup>l,11</sup>, D. Zerwas<sup>l</sup>,  
 B. Dekhissi<sup>m</sup>, J. Derkaoui<sup>m</sup>, A. El Kharrim<sup>m</sup>, F. Maaroufi<sup>m</sup>  
 W. Cleland<sup>o</sup>, D. Lacour<sup>n</sup>, B. Laforge<sup>n</sup>, I. Nikolic-Audit<sup>n</sup>,  
 Ph. Schwemling<sup>n</sup>, H. Ghazlane<sup>p</sup>, R. Cherkaoui El Moursli<sup>q,r</sup>,  
 A. Idrissi Fakhr-Eddine<sup>q</sup>, M. Boonekamp<sup>s</sup>, N. Kerschen<sup>s</sup>,  
 B. Mansoulié<sup>s</sup>, P. Meyer<sup>s</sup>, J. Schwindling<sup>s</sup>, B. Lund-Jensen.<sup>t</sup>

<sup>a</sup>*Laboratoire de Physique de Particules (LAPP), Université de Savoie,  
 CNRS/IN2P3, Annecy-le-Vieux Cedex, France.*

<sup>b</sup>*Brookhaven National Laboratory (BNL), Upton, NY 11973-5000, USA.*

<sup>c</sup>*Faculté des Sciences Aïn Chock, Casablanca, Morocco.*

<sup>d</sup>*Southern Methodist University, Dallas, Texas 75275-0175, USA.*

<sup>e</sup>*European Laboratory for Particle Physics (CERN), CH-1211 Geneva 23, Switzerland.*

<sup>f</sup>*Laboratoire de Physique Subatomique et de Cosmologie, Université Joseph Fourier, IN2P3-CNRS, F-38026 Grenoble, France*

<sup>g</sup>*Nevis Laboratories, Columbia University, Irvington, NY 10533, USA.*

<sup>h</sup>*Physics Department, Universidad Autónoma de Madrid, Spain.*

<sup>i</sup>*Centre de Physique des Particules de Marseille, Univ. Méditerranée, IN2P3-CNRS, F-13288 Marseille, France.*

<sup>j</sup>*Dipartimento di Fisica dell’Università di Milano and INFN, I-20133 Milano, Italy.*

<sup>k</sup>*Budker Institute of Nuclear Physics, RU-630090 Novosibirsk, Russia.*

<sup>l</sup>*LAL, Univ Paris-Sud, IN2P3/CNRS, Orsay, France.*

<sup>m</sup>*Laboratoire de Physique Théorique et de Physique des Particules, Université Mohammed Premier, Oujda, Morocco.*

<sup>n</sup>*Universités Paris VI et VII, Laboratoire de Physique Nucléaire et de Hautes Energies, F-75252 Paris, France.*

<sup>o</sup>*Department of Physics and Astronomy, University of Pittsburgh, Pittsburgh, PA 15260, USA.*

<sup>p</sup>*Centre National de l’Énergie, des Sciences et Techniques Nucléaires, Rabat, Morocco.*

<sup>q</sup>*Faculty of Science, Mohamed V-Agdal University, Rabat, Morocco.*

<sup>r</sup>*Hassan II Academy of Sciences and Technology, Morocco.*

<sup>s</sup>*CEA, DAPNIA/Service de Physique des Particules, CE-Saclay, F-91191 Gif-sur-Yvette Cedex, France.*

<sup>t</sup>*Royal Institute of Technology, Stockholm, Sweden.*

---

## Abstract

The construction of the ATLAS electromagnetic liquid argon calorimeter modules is completed and all the modules are assembled and inserted in the cryostats. During the production period four barrel and three endcap modules were exposed to test beams in order to assess their performance, ascertain the production quality and reproducibility, and to scrutinize the complete energy reconstruction chain from the readout and calibration electronics to the signal and energy reconstruction. It was also possible to check the full Monte Carlo simulation of the calorimeter. The analysis of the uniformity, resolution and extraction of constant term is presented. Typical non-uniformities of 5 % and typical global constant terms of 6 % are measured for the barrel and end-cap modules.

*Key words:* Calorimeters, High Energy Physics, Particle Detectors, Energy Resolution and Uniformity

## INTRODUCTION

The large hadron collider (LHC) will collide 7 TeV proton beams with luminosities ranging from  $10^{33}$  to  $10^{34}\text{cm}^{-2}\text{s}^{-1}$ . The very high energy and luminosity foreseen will allow to investigate the TeV scale in search for new phenomena beyond the Standard Model. Reaching such performance is an outstanding challenge for both the collider and the detectors.

The electromagnetic calorimeter of the ATLAS detector, one of the two multi purpose experiments at LHC, is a lead and liquid argon sampling calorimeter with accordion shaped absorbers. In its dynamic range covering the few GeV up to the few TeV domain an excellent measurement of the energy of electrons and photons is required in order to resolve potential new particle resonances, and to measure precisely particle masses and couplings.

One of the salient benchmark processes that has guided the design of the electromagnetic ATLAS calorimeter is the Higgs boson production with subsequent decay into a pair of photons. This event topology will be observable only if the Higgs boson mass is smaller than  $\sim 150$   $\text{GeV}/c^2$ . In this channel the capabilities of the calorimeter in terms of photon pointing resolution and  $\gamma/\pi^0$  discrimination are of chief concern. An excellent and uniform measurement of the photon energy is essential. Another process involving the Higgs boson where it decays to a pair of Z bosons and subsequently into four electrons also requires a uniform measurement of the electron energy over a large dynamic range. Finally, among the processes which will require the most ac-

---

<sup>1</sup> Now at university of Geneva, switzerland.

<sup>2</sup> Now at Rutherford Appleton Laboratory (RAL), Chilton, Didcot, OX11 0QX, United Kingdom.

<sup>3</sup> Now at university of Toronto, Ontario, Canada.

<sup>4</sup> Visitor from LPHEA, FSSM-Marrakech (Morroco).

<sup>5</sup> Deceased.

<sup>6</sup> Also at KFKI, Budapest, Hungary. Supported by the MAE, France, the HNCfTD (Contract F15-00) and the Hungarian OTKA (Contract T037350).

<sup>7</sup> Corresponding author, E-mail: kado@lal.in2p3.fr

<sup>8</sup> Now at Queen Mary, University of London.

<sup>9</sup> Now at LAL, Univ Paris-Sud, IN2P3/CNRS, Orsay, France.

<sup>10</sup> Now at Faculté de Physique, Université des Sciences et de la technologie Houari Boumediène, BP 32 El-Alia 16111 Bab Ezzouar, Alger, Algérie.

<sup>11</sup> Now at CERN, Geneva, Switzerland.

curate knowledge of the electron energy is the W mass measurement whose goal precision is  $\sim 0.2\%$ . For all these processes the constant term  $b$  of the three main resolution elements:

$$\frac{\sigma_E}{E} = \frac{a}{\sqrt{E}} \oplus b \oplus \frac{c}{E}$$

(where  $c$  and  $a$  are the noise and stochastic terms respectively) plays an important role. It arises from various sources encompassing the calibration and readout electronics, the amount of material before and in the calorimeter, the energy reconstruction scheme and its stability in time. The  $c$  term comprises the electronic noise and the pile-up.

Many years of R&D work [1,2,3,4,5] have led to the ATLAS calorimeter design whose first performance assessments on pre-production modules were reported in [6,7]. Since then, modifications were made in order to improve the production, the quality control and the performance of the calorimeter modules. During the three years of module construction, four barrel and three endcap modules have been exposed to electron beams in the North Area at CERN's SPS. The primary aim was to assess the quality of the production by measuring the response uniformity over the complete acceptance. However, these measurements have led to numerous further improvements of the calibration, signal reconstruction and the simulation of the calorimeter.

This paper reports on measurements of the uniformity and a study of the different contributions to the constant term of the electron energy resolution for barrel and endcap modules exposed to high energy electron beams. The actions taken to optimize the electron energy resolution and in particular the uniformity of the response are also described. Finally a review of all sources of non-uniformities is presented.

The paper is organized as follows. In Sec. 1 the main features of the calorimeter modules are described and the differences with respect to the pre-production modules are briefly presented. A description of the readout and calibration electronics is then given in Sec. 2. The signal reconstruction, including cross talk issues is also presented. The beam test setups are described in section 3. Finally the barrel and endcap analysis and results are presented in Sec. 4 and Sec. 5.

## 1 CALORIMETER MODULES DESCRIPTION

The ATLAS electromagnetic calorimeter is a lead and liquid argon sampling calorimeter using an accordion geometry for gaps and absorbers. It is composed of a cylindrical barrel centered on the beam and two endcaps. The usual

slightly modified polar coordinate system is used, where the  $z$ -axis coincides with the beam axis,  $\phi$  is the azimuthal angle and the polar angle  $\theta$  is replaced by the pseudo rapidity  $\eta = -\ln(\tan\theta/2)$ . A detailed description of the detector can be found in [8,9,10,11]. The main characteristics are, however, described hereafter.

### 1.1 Barrel Modules Description

The ATLAS barrel calorimeter is divided in two half barrels covering the positive and the negative pseudo rapidities, from  $|\eta| = 0$  to  $|\eta| = 1.475$ . The inner and outer diameters are about 2.8 m and 4 m. Each half barrel consists of sixteen 3.2 meter long modules made of 64 accordion shaped absorbers interleaved with readout electrodes. Modules are made of two types of electrodes denoted A and B covering the pseudo rapidity ranges  $[0, 0.8]$  and  $[0.8, 1.475]$  separated by 2.5 mm at the transition point. The construction and testing of these modules is reported in [9]. In each of these regions the lead thickness is different in order to maintain an approximately constant stochastic term of the energy resolution (1.53 mm for  $|\eta| < 0.8$  and 1.13 mm for  $|\eta| > 0.8$ ). The drift gap on each side of the electrode is 2.1 mm which corresponds to a total drift time of about 450 ns at 2 kV. The electrodes are segmented in three compartments in depth (front, middle, back). The first section with narrow strips along  $\eta$ , ends after 4 radiations lengths ( $X_0$ ), while the second stops after 22  $X_0$ . The total thickness of the module varies as a function of  $\eta$  between 22 and 33  $X_0$ . Summing boards, plugged on the electrodes, perform the signal summation in  $\phi$  : 16 adjacent electrodes are summed for a strip cell and 4 electrodes for middle and back cells. The granularity of the different compartments are shown in Table 1 for  $|\eta| < 1.475$ . A presampler is placed in front of the electromagnetic calorimeter inside the cryostat. Each unit provides coverage in  $|\eta|$  from 0 to 1.52 and covers a region of  $\Delta\phi = 0.2$ . The signal is sampled in a thin active layer of 11 mm of liquid argon with a readout cell granularity of  $\Delta\eta \times \Delta\phi = \sim 0.025 \times 0.1$  [11]. In total, there are 3424 readout cells per module. The high voltage is supplied independently on each side of the electrode by sectors of  $\Delta\eta \times \Delta\phi = 0.2 \times 0.2$  corresponding to 32 electrodes.

Four barrel modules (two of each half barrel) were exposed in the H8 beam test line, namely M13, M10, P15 and P13. They are now part of the final ATLAS calorimeter. However, because of the incorrect mounting of the support of a cerenkov counter, non homogeneous material was added in the beamline while the module M13 was being tested. As a consequence its performance could not be thoroughly measured. Therefore, only results for M10, P13 and P15 are presented.

## 1.2 Endcap Modules Description

The ATLAS electromagnetic endcap calorimeter (EMEC) covers the rapidity region from 1.375 up to 3.2 and consists of 2 wheels, one on each side of the electromagnetic barrel. Each wheel, divided into eight wedge-shaped modules, is 63 cm thick with internal and external radii of about 30 cm and 2 m. For technical reasons, it is divided in one outer ( $1.375 < |\eta| < 2.5$ ) and one inner ( $2.5 < |\eta| < 3.2$ ) wheel, both projective in  $\eta$ . The crack between the wheels is about 3 mm wide and is mainly filled with low density material. In  $\phi$ , one outer (inner) wheel module is made of 96 (32) accordion shaped absorbers interleaved with readout electrodes, covering a range of  $\Delta\phi = 2\pi/8$ . Accommodating the accordion shape in the endcap region induces a quite complicated geometry. Most of the design parameters vary along the radius direction (corresponding to  $\eta$ ) : liquid argon gap, sampling fraction, accordion wave amplitudes or folding angles. A continuously varying high voltage setting along  $\eta$ , would partially compensate for this and imply an almost  $\eta$ -independent detector response. However, the high voltage is set by steps. The outer (inner) wheel is divided into seven (two) high voltage sectors. In each of them a residual  $\eta$ -dependence of the response will need to be corrected.

In the region devoted to precision physics, where the tracking information is available ( $1.5 < |\eta| < 2.5$ ), the depth segmentation is similar to the barrel one. At large rapidity, there are only two compartments in depth. Twelve adjacent electrodes are summed for one strip cell and 3 (4) for middle and back cells in the outer (inner) wheel. The segmentation of the EMEC is summarized in Table 1. There are 3888 readout cells per module. HV boards distribute the high voltage to  $\phi$ -sectors of 24 (4) electrodes in the outer (inner) wheel, independently on each side.

Three endcap modules where exposed to the H6 beam line namely ECC0, ECC1 and ECC5.

## 1.3 Design modifications

Following the construction and the beam tests of the prototype modules 0 [6,7], a few design modifications have been implemented :

- The high voltage is distributed on the electrodes by resistors made of resistive paint silkscreened on the outer copper layer of the electrodes. The role of these resistors is also to limit the current flowing through the readout electronics in case of an unexpected discharge of the calorimeter cell. Some of these resistors located near the electrode bends were displaced in order

Modules	$\eta$ range	Front	Middle	Back
Barrel	[0.0,0.8]& [0.8,1.35]	$0.003 \times 0.1$	$0.025 \times 0.025$	$0.050 \times 0.025$
	[1.35,1.4]	$0.003 \times 0.1$	$0.025 \times 0.025$	-
	[1.4,1.475]	$0.025 \times 0.1$	$0.075 \times 0.025$	-
EC	[1.375,1.425]	$0.050 \times 0.1$	$0.050 \times 0.025$	-
	[1.425,1.5]	$0.025 \times 0.1$	$0.025 \times 0.025$	-
	[1.5,1.8]	$\sim 0.003 \times 0.1$	$0.025 \times 0.025$	$0.050 \times 0.025$
	[1.8,2.0]	$\sim 0.004 \times 0.1$	$0.025 \times 0.025$	$0.050 \times 0.025$
	[2.0,2.4]	$\sim 0.006 \times 0.1$	$0.025 \times 0.025$	$0.050 \times 0.025$
	[2.4,2.5]	$0.025 \times 0.1$	$0.025 \times 0.025$	$0.050 \times 0.025$
EC Inner	[2.5,3.2]	-	$0.1 \times 0.1$	$0.1 \times 0.1$

Table 1. *Granularity ( $\Delta\eta \times \Delta\phi$ ) of calorimeter cells in the electrodes A and B of the barrel modules and the outer and inner wheels of the endcaps (EC).*

to avoid breaking during the bending process. This lead to a change of the bending process of the barrel electrodes [10].

- On the prototype, an increased cross talk and pulse shape deformation was observed every 8 (4) channels in the barrel (endcap). This effect was traced back to the absence of ground on one side of some signal output electrode connectors. These missing contacts were added in the production electrode circuits.
- Summing and motherboards<sup>12</sup> of the endcap were redesigned to reduce the inductive cross talk to an acceptable level (<1 %) [13].
- Precise calibration resistors (0.1 % accuracy) are located on the mother board. It appears that if an accidental HV discharge occurs, a large fraction of the energy released could damage these resistors, thus preventing any calibration of the cell. Diodes were added on the signal path to protect these resistors for the middle and back cells where the detector capacitances are the largest. For the strips section such a protection scheme [14] could not be installed, but the smaller detector capacitances reduce the risk of damage.
- Finally for the endcap construction, the cleanliness and humidity regulation of the stacking room were improved. The honeycomb spacers, which keep the electrodes centered on the gap, were modified to ensure a better positioning. They were measured and tested under high voltage before stacking and checked at the nominal high voltage settings after each gap stacking.

<sup>12</sup> Motherboards, plugged on top of the summing boards, ensure the signal routing and the distribution of calibration signals.

## 1.4 Quality control measurements

During the production a number of quality control measurements was performed on all barrel modules. The lead thickness, the argon gap width and some electrical parameters linked to the electrode design are key parameters for the response of the calorimeter. These measurements were done to ensure that all components were made with the required precision. Similar measurements were also performed on the endcap modules, details of the gap variation will be discussed in the endcap data analysis section.

### 1.4.1 Absorber thickness

Before assembling the modules, the thickness of all lead sheets were measured by means of an ultra sound system, producing a map with a  $5 \times 5 \text{ cm}^2$  granularity [9,15]. These maps have been used to select the stacking order of the lead sheets to minimize the thickness fluctuations across each module. For each lead plate the measurements are averaged projectively along the shower axis. As most of the shower energy is shared by five absorbers, the thicknesses for  $|\eta| < 0.8$  ( $|\eta| > 0.8$ ) normalized to their nominal values are averaged in a sliding window of five consecutive absorbers. Finally to emulate the energy profile within the electron cluster, each average is weighted according to a typical electron energy deposition shape. In Fig. 1 the variation of the normalized lead thickness as a function of the middle cell  $\eta$  index (as described below) for the modules P13, P15 and M10 is shown. The dispersions do not exceed 0.3 % per module.

For barrel modules the  $\eta$  middle cell indices run from 0 to 54 covering the pseudo rapidity range from 0 to 1.35. The  $\phi$  cell indices correspond to increments in azimuthal angle of  $\pi/128$ . They range between 0 and 15. For endcap modules the middle cell  $\eta$  index used covers the region in pseudo rapidity from 1.375 up to 3.2 with indices ranging from 0 to 50. The  $\phi$  middle cell indices increment is the same as that of the barrel modules for the outer wheel and  $\pi/32$  for the inner wheel. In the  $\phi$  direction these indices range from 0 to 31 in the outer wheel and from 0 to 7 in the inner wheel.

Similar measurements were also performed on endcap modules. The dispersions of the normalized lead thicknesses are within 0.3 % for all modules.

### 1.4.2 Gap dispersion

At the end of modules stacking, the gap capacitance of each sector of  $\Delta\eta = 0.2$ , corresponding to eight middle layer cells, was measured. In each of these sectors, the capacitances were normalized to their average value and the gap

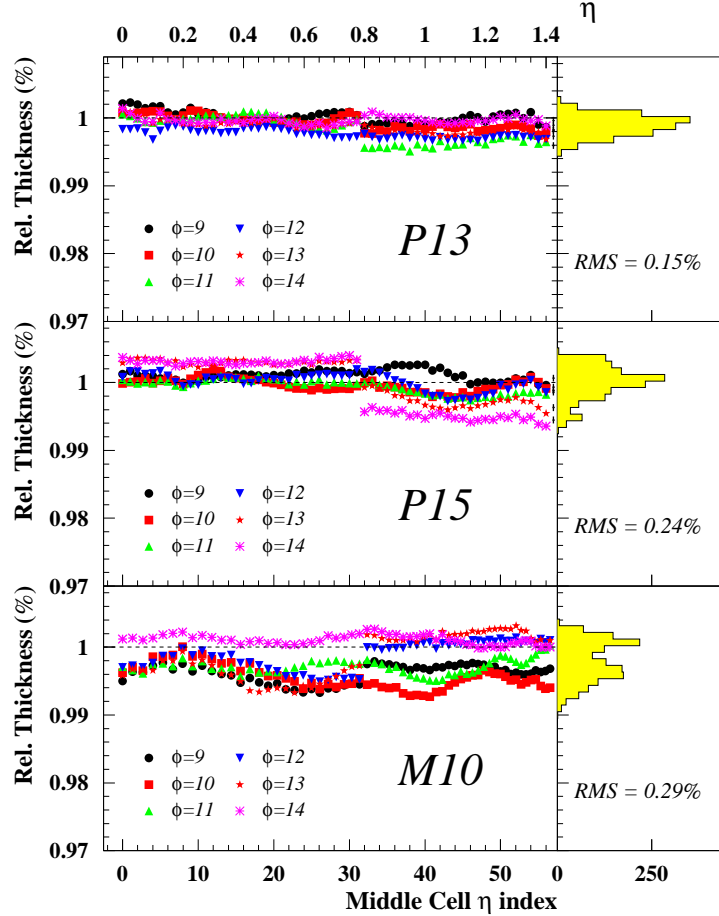


Fig. 1. Weighted average lead absorber thickness per middle cell as a function of the middle cell  $\eta$  index for various  $\phi$  regions. The distribution of the measurements is also shown and the dispersion is indicated.

variations were extracted. Similarly to the lead thickness, most of the shower is shared in a few gaps. Using a typical electromagnetic lateral shower energy profile, a sliding energy-weighted-gap was calculated. Its dispersion is summarized in Table 2 for the 3 barrel modules. While P13 and P15 show similar results, the module M10 has a larger dispersion. This effect was explained by the use of electrodes made before and after the modification of the bending process.

Module	P13	P15	M10
Total	0.62 %	0.64 %	1.66 %
FT0 subset	0.58 %	0.39 %	1.41 %

Table 2. Dispersions of the weighted average gaps for each barrel module P13, P15 and M10. The FT0 subset corresponds to the region instrumented with the readout electronics used in the analyses described in Sec. 2.1 and Sec. 4.7.

Since in endcap modules the size of the gap is not constant, the precise measurement of the gap is very important in order to evaluate the electron clusters energies. The gaps were also indirectly estimated from the cell capacitance measurements in the endcap modules [16]. These results are discussed in Sec. 5.2.2.

## 2 CALIBRATION AND SIGNAL RECONSTRUCTION

### 2.1 Readout Electronics

As described in Sec 1.1, the readout signal consists of the sum of signals measured in various electrodes. The analog sum is made by summing boards connected at both ends of the electrodes; at the front for the strip compartment and at the back for the middle and back compartments. The motherboards, plugged on top of the summing boards, send the signals through cold cables out to the front-end boards placed outside the cryostat at room temperature. The readout electronics are located in crates at both ends of the cryostat. To extract the calorimeter signals from inside the cold vessel the feedthrough (FT) connexion devices are used [8]. Two FTs are required for each barrel module. Each of them covers half a module in  $\phi$ . Three FTs are required for each endcap module. The readout front-end electronics crates are placed on top of the FT devices. In particular, for the beam test barrel modules there are two FT devices covering a half barrel each. The regions covered are denoted FT-1 and FT0.

In the front-end boards, signals are amplified and shaped through a bipolar  $CR \cdot RC^2$  filter with a time constant  $\tau_S = 15$  ns, then sampled every 25 ns and digitized. The shaping consists in one derivation (CR) to form a bi-polar signal and two integrations (RC) allowing both to reduce the impact of the pile-up and electronic noise. The choice of shaping time constant results from the minimization of the electronic noise and pile-up.

The energy dynamical range covered by the calorimeter signals requires 16 *bits* whereas the available Analog-to-Digital Converter (ADC) modules are limited to 12 *bits*. To produce the adequate signal range the shapers produce three signals amplified in three different gains low, medium and high in the ratio of respectively 1, 9.3 and 93. All signals are then stored in an analog pipeline awaiting for a first level trigger decision. When the decision is made the signals either from the three gains or from the most suited one according to a hardware

gain selection are digitized. In the beam test setup the signals are directly readout while in the full ATLAS configuration they are sent to a higher level firmware system where the energy is fully reconstructed for further use both higher level trigger and in physics analysis.

## 2.2 Detector Electrical Properties

A detector cell can be seen as a resonant circuit as illustrated in Fig. 2. The resonance frequency is linked to the capacitance and inductance of the detector cell and summing boards. These resonance frequencies have been measured on the assembled calorimeter for each module using a network analyzer [17]. In Fig. 3 the results for the module P13 and P15 filled with liquid argon are displayed. The structure is mainly due to the variation of the inductance along  $\eta$  resulting from the electrode design in which the lines serving to extract the signal of middle cells varies with  $\eta$ . The differences along  $\phi$  reflect non uniformities of the summing boards. The  $\phi$  dispersion of these frequencies amounts to about 1.2 %, which is compatible with the expected gap variation.

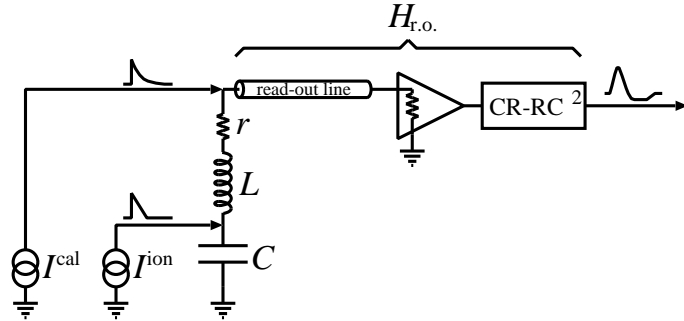


Fig. 2. Simple schematic electrical model of the cell electronic environment. The shape of the calibration and ionization signals is also illustrated along with the output pulse. Here  $C$  is the cell capacitance,  $L$  the inductive path of the signal and  $r$  is the resistance.

Similar measurements were made on endcap modules yielding frequencies increasing as a function of  $\eta$  from 20 to 40 MHz.

## 2.3 Calibration System

The calorimeter is equipped with an electronic calibration system [18] that allows prompt measures of the gain and electrical response of each readout cell. This system is based on the ability to inject into the detector an exponential<sup>13</sup>

<sup>13</sup> A small offset  $f_s$  is present, due to the resistive component of the inductance in the calibration board. Typically  $f_s \simeq 7\%$ .

calibration pulse of known amplitude ( $I^{\text{cal}}(t)$ ) that mimics the ionization pulse generated by the particles hitting the detector:

$$I^{\text{cal}}(t) = I_0^{\text{cal}} \theta(t) \left[ f_s + (1 - f_s) e^{-\frac{t}{\tau_c}} \right] \quad (1)$$

with a time decay constant  $\tau_c \simeq 350$  ns ( $\theta(t)$  is the unit step function). The calibrated pulse shape ( $g^{\text{cal}}(t)$ ) is reconstructed using programmable delays by steps of about 1 ns.

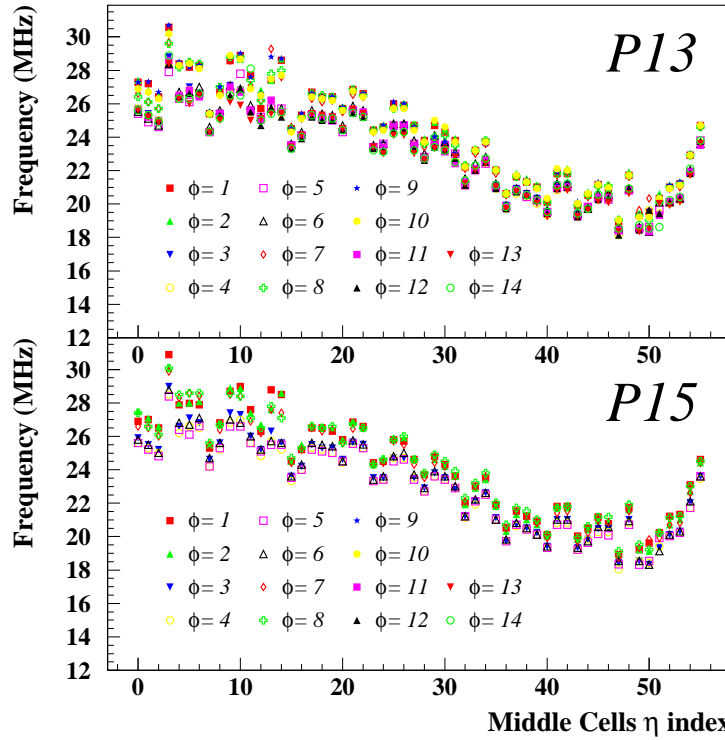


Fig. 3. Resonance frequencies for modules P13 and P15 as a function of the  $\eta$  index for all middle cells for various  $\phi$  regions.

The signal is generated by means of a digital-to-analog converter (DAC) which controls the input current. Its value is proportional to the DAC requested. A constant very small parasitic charge injection DAC value is present due to parasitic couplings. It was measured and its value accounted for.

The signal is produced in calibration boards placed in the front-end crates. It is then carried into the cold vessel and distributed to the electrodes through injection resistors  $R_{\text{inj}}$  which are precise at the 0.1 % level. These resistors are placed on the motherboards.

A non uniformity of the calibration signals would affect the uniformity *in fine*. All potential sources of non uniformity affecting the calibration signal have thus been independently measured. The main ones are:

- (i) the pulsers: each line is measured on the calibration board directly. A relative dispersion of 0.19 % is found.
- (ii) calibration resistors: each calibration resistor is measured and a relative dispersion of 0.08 % is found for barrel modules and 0.05 % in the endcaps.
- (iii) cables: The attenuation by skin effect which is proportional to the cable length is corrected in average, however a small relative dispersion of at most 0.1 % could still impact the energy uniformity.

The overall precision of the calibration system is  $\sim 0.23\%$ .

## 2.4 Energy Reconstruction

When electrons and photons hit the calorimeter they interact within the lead absorbers producing an electromagnetic cascade. Its charged component ionizes the liquid argon in the gaps, inducing a triangular current signal [19] ( $I^{\text{ion}}(t)$ ):

$$I^{\text{ion}}(t) = I_0^{\text{ion}} \theta(t) \theta(T_D - t) \left(1 - \frac{t}{T_D}\right) \quad (2)$$

whose length equals the drift time,  $T_D \simeq 450$  ns (in the endcaps the drift time decreases from 550 down to 250 ns as a function of  $\eta$ ).

The ionization signal amplitude is reconstructed in each gain from the five digitized samples  $S_k$ , to which the pedestals have been subtracted (see Sec. 2.4.1), located around the peak, using the *optimal filtering* (OF) technique [20]:

$$\begin{cases} A = \sum_{k=1}^5 a_k S_k \\ A \times \tau = \sum_{k=1}^5 b_k S_k \end{cases} \quad (3)$$

where  $A$  is the amplitude estimator and  $\tau$  is the signal arrival time estimate with respect to the readout clock. The coefficients  $a_k$  and  $b_k$  are chosen in order to minimize the effect of electronic noise. They are analytically calculated through a Lagrange multiplier technique [20], provided one knows for each readout cell the normalized shape of the ionization signal  $g^{\text{ion}}(t)$ , its derivative and the noise time autocorrelation. The latter is computed from the data acquired during the pedestal runs.

The cell energy is then reconstructed from the cell signal amplitude  $A$  using the following prescription:

$$E_{vis}^{cell} = \frac{1}{f_{I/E}} \xi A$$

This formula can be read as the sequence of the following operations: (i) the conversion of the signal in ADC counts  $A$  into a current in  $\mu\text{A}$  corresponding to the calibration of the readout electronics with the function  $\xi$ ; (ii) the conversion factor from current to energy  $f_{I/E}$ .

#### 2.4.1 Pedestal Subtraction

During the running period, data in absence of beam were taken daily to assess the level of signal without any energy deposition in each cell for all gains of all modules. In addition, in order to address precisely the more subtle possible variations on a run-by-run basis the pedestals can be evaluated from triggers taken at random during the run. The variations between no-beam runs and random triggers are in general negligible and thus not taken into account but for a few runs small instabilities, in particular in the presampler, could produce a detectable bias in energy not exceeding 20 MeV. The subtraction of pedestals is done on all signal samples ( $S_k$ ) before applying the *optimal filtering* method.

#### 2.4.2 Calibration Procedure

The calibration procedure establishes the correspondence between a signal readout in ADC counts and a known injected current in the cell in  $\mu\text{A}$ . Calibration data were taken approximately twice daily throughout the running period.

The procedure consists in fitting the ADC response as a function of the DAC values knowing that the injection currents vary linearly with the DAC values. A second order polynomial form  $\xi$  is used. The higher order fine structure of the non linear response of the calibration is not relevant here. The aforementioned function also contains a DAC to current constant conversion factor.

#### 2.4.3 Current to Energy conversion Factor

Estimating from first principles the relation between the measured current and the energy is an intricate task, as numerous complex effects can introduce biases as detailed in [21]. However, the simplified model estimation of  $f_{I/E} \sim$

14.4 nA/MeV in the barrel accordion in the straight sections (7 % less when taking into account the folds [22]), yields a result accurate to the few percent level. This value is in agreement with a more precise calculation in which the detailed cell electric fields and recombination effects are taken into account. In the case of the analysis of the barrel modules where a complete and thorough simulation of the calorimeter was used a more precise estimate of the  $f_{I/E}$  factor is obtained from a comparison of the Monte Carlo simulation with the data (see Sec. 4.5).

## 2.5 Signal Reconstruction

The normalized response  $g^{\text{ion}}(t)$  of the system to the ionization current differs from the response  $g^{\text{cal}}(t)$  to a calibration current because the two pulses are respectively triangular and exponential, and while the former is generated inside the detector, the latter is injected in the cell from one end of the detector and reaches the inside through an inductive path<sup>14</sup>. Typical shapes of the two signals at the end of the readout chain are shown in Fig. 4.

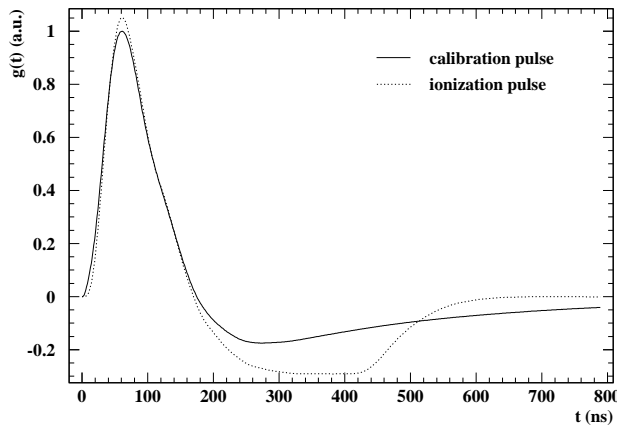


Fig. 4. Normalized calibration  $g^{\text{ion}}(t)$  and ionization  $g^{\text{cal}}(t)$  pulses.

The difference between the calibration and the ionization pulses can be analytically described by modeling the liquid argon readout cell as a lumped  $rLC$  model (see Fig. 2), where the two currents share the same readout chain while being generated in different places. After taking into account the analytical descriptions (2) and (1), the relation between the current shapes is [24,25,26]:

<sup>14</sup> The effect is not negligible, as it affects the amplitude ratio of the ionization and calibration waveforms by approximately 0.15 %/nH, and the inductance value varies throughout the detector from 35 to 55 nH [23].

$$g^{\text{ion}}(t) = g^{\text{cal}}(t) \times \mathcal{L}^{-1} \left[ \frac{sT_{\text{D}} - 1 + e^{-sT_{\text{D}}}}{s^2 T_{\text{D}}} \frac{s(1 + s\tau_{\text{c}})}{f_s + s\tau_{\text{c}}} \right] \\ \times \mathcal{L}^{-1} \left[ \frac{1}{1 + s^2 LC + srC} \right] \quad (4)$$

where the normalized ionization signal  $g^{\text{ion}}(t)$  can be inferred from the observed calibration signal  $g^{\text{cal}}(t)$  by means of time-domain convolutions with functions that depend on the parameters  $T_{\text{D}}, \tau_{\text{c}}, f_s, LC, rC$  (where  $\tau_{\text{c}}, f_s$  are the calibration time constant and a calibration offset) only using the inverse Laplace transform  $\mathcal{L}^{-1}$  with the Laplace variable  $s$ . The resonance frequencies displayed in Fig. 3 correspond to the standard oscillator circuit thus  $f = 1/2\pi\sqrt{LC}$ . The evaluation of  $g^{\text{ion}}(t)$  is completely independent of any details of the read-out chain.

For the barrel modules the drift time  $T_{\text{D}}$  can be estimated with various methods [25,27,28], while the parameters  $\tau_{\text{c}}, f_s$  and  $LC, rC$  can be extracted either by analyzing the observed signals or from direct measurements. In the end-caps  $T_{\text{D}}$  varies continuously with  $\eta$ , it was thus considered as a parameter. Two strategies were developed for the test beam, as described in the next subsections.

### 2.5.1 Semi-predictive approach

The following method [24,26] has been used to reconstruct the energy for the prototype modules [6,7] and for all tested production modules.

At the test beam, the electrons reach the calorimeter at random time with respect to the sampling clock<sup>15</sup> (asynchronous events). It is thus possible to sample the ionization signal every nanosecond, similarly to what is done for the calibration signal. However, the signal shape obtained from direct observation is imprecise, due to the low statistics and the large fluctuations in the shower development. Moreover, its normalization is arbitrary.

The parameters  $\tau_{\text{c}}$  and  $f$  are measured directly on the calibration board before its installation on the detector.

The parameters  $LC$  and  $rC$  are obtained from a fit of the predicted ionization signal, as obtained from equation (4), to the observed one. In the fit, two more parameters are allowed to vary in order, to account for a time shift between the two signals and for the amplitude scale factor. Once  $LC$  and  $rC$  are found,

---

<sup>15</sup> The time between the trigger given by a scintillator coincidence and the 40 MHz clock edge is measured for each event.

the predicted ionization signal has the correct normalization and can be used to evaluate the OF coefficients.

### 2.5.2 Fully predictive method

This method is an alternative to the one described previously: it has the advantage of being based on calibration data only, thus not relying on a direct knowledge of ionization pulses from asynchronous events. It relies on the observation of long enough calibration signals: up to 32 digitized samples can be acquired, corresponding to a maximum length of 800 ns. The details are fully described in [25], therefore only an overview is given here.

The exponential decay time can be extracted from a fit of the tail of the calibration signal. The offset  $f$  can be estimated as follows: if the injected  $I^{\text{cal}}(t)$  was a step-function, then the tail of the shaped signal would be minimal. The detector response to an injected step could be calculated, by means of a time-domain convolution between  $g^{\text{cal}}(t)$  and a function of time which depends on the parameters  $\tau_c$  and  $f$ . Once  $\tau_c$  is found, the best value for  $f$  is chosen as that minimizing the tail of the response function.

The parameters  $LC$  and  $rC$  are extracted from a frequency analysis of the transfer function, which exhibits a minimum for angular frequency  $\omega = \frac{1}{\sqrt{LC}}$ . This is achieved either by a direct use of a fast Fourier transform, or with techniques similar to that described for the extraction of  $f$  — here the characteristics of the detector response to a sinusoidal injected signal are exploited: the best value for  $\omega$  is that minimizing the oscillations in the tail.

Such a technique has been applied to a restricted region of a production module where the 32-samples-calibration data were made available (half a module for the Middle and Back compartments, and only a  $\Delta\eta \times \Delta\phi = 0.2 \times 0.2$  sector for the Strips). The residuals between the observed and predicted ionization signal are at the level of 1 % (0.2 % in the peak region). The agreement in the timing between the OF reconstruction and the scintillator measurement is within 350 ps.

For various runs taken on a reduced region of the barrel modules both methods were applied. The comparison of the two methods is used to estimate the possible biases due to the reconstruction method chosen. The results of this comparison are given in Sec. 4.11.3.

### 2.5.3 Prediction of the Physics to Calibration Amplitude Ratio

Since the predicted signal and calibration shapes are different, the response amplitude to a normalized input signal will be different. This difference must

be taken into account in order to correctly convert ADC counts into energies. It is done using the prediction of the physics to calibration amplitude ratio, namely  $M_{phys}/M_{cal}$ . This ratio varies with pseudo rapidity. These variations are displayed in Fig. 5 and 6 for the barrel and endcap modules respectively.

The barrel strips  $M_{phys}/M_{cal}$  is reasonably consistent with 1, whereas for middle cells the prediction to calibration amplitude ratio increases systematically with  $\eta$  up to the middle cell  $\eta$  index 48. These variations are consistent with the resonance frequencies measured and presented in Sec. 2.2. A similar effect is observed in endcap modules.

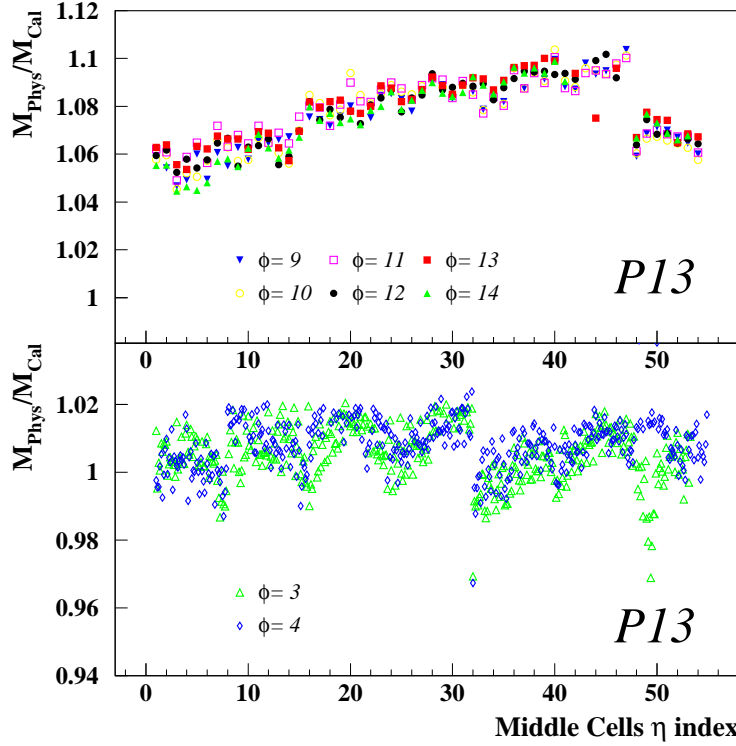


Fig. 5. Bias in the signal reconstruction method as derived for the barrel P13 module at all middle  $\eta$  indices and azimuthal angles, for middle cells (upper plot) and strips (lower plot).

#### 2.5.4 Energy Dependence with Time

Contrary to what will be the case in the ATLAS experiment and due to the time spread of electron bunches, in the test beam the time phase is essentially random. For all barrel and endcap modules it was checked that in the energy reconstruction scheme no bias is observed as a function of the time phase.

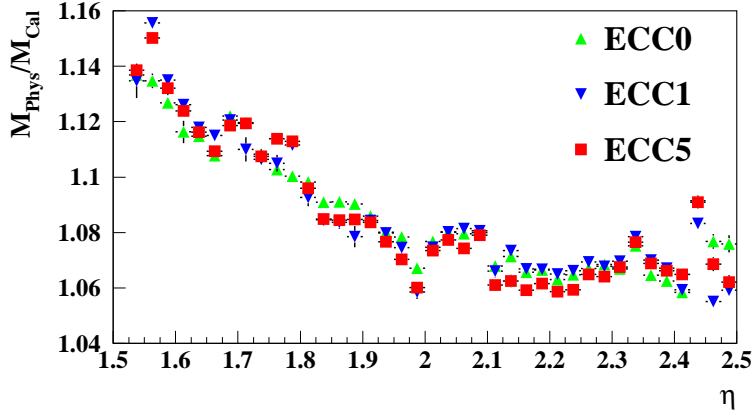


Fig. 6. *Bias in the signal reconstruction as derived for all tested EMEC modules (ECC0, ECC1 and ECC5) for middle cells averaged in the azimuthal direction as a function of the pseudo rapidity.*

## 2.6 Cross Talk Issues

### 2.6.1 Module Electrodes Cross Talks

Various cross talk effects inherent to the design of calorimeter cells or due to the readout electronics are present in the calorimeter. A complete description of the origin of these effects can be found in [12,13]. These unavoidable effects have been measured mainly using calibration signals [29,30,31]. A summary of the measurements of the typical cross talks are given in Table 3 for both the barrel and the endcap electrodes. The cross talks are here defined as peak-to-peak, *i.e.*, the maximum amplitude of the cross talk is normalized to the signal amplitude. All the effects described here are those measured in nearest neighbors, second order effects are negligible, except for the secondary cross talk between a strip and its next to nearest neighbor with a peak-to-peak value of 0.9 % for barrel and 0.5 % for endcap electrodes.

Among these cross talk effects mainly two will affect the energy reconstruction: the strips capacitive cross talk and the middle-back inductive cross talk.

The strips cross talk effect is due to the thin separation between the finely segmented cells of the first compartment of the calorimeter, the fine segmentation is necessary for the  $\pi^0/\gamma$  separation, for a precise estimation of the pseudo rapidity of the impact point and for the estimation of the photon pointing direction. This effect non trivially affects the calibration and the signal reconstruction. Its treatment is described in Section 2.6.2.

The cross talk between the middle and the back compartment results from a

Module Part	Electrode A			Electrode B		
Compartment	Front	Middle	Back	Front	Middle	Back
Front	6.9 % <sup>2</sup>	0.07 % <sup>1</sup>	0.04 % <sup>4</sup>	6.9 % <sup>2</sup>	0.09 % <sup>1</sup>	0.04 % <sup>4</sup>
Middle	0.07 % <sup>1</sup>	1.5 % <sup>2+3</sup>	0.5 % <sup>3+2</sup>	0.09 % <sup>1</sup>	1.5 % <sup>2+3</sup>	0.7 % <sup>3+2</sup>
Back	0.04 % <sup>4</sup>	0.5 % <sup>3+2</sup>	1.9 % <sup>3</sup>	0.04 % <sup>4</sup>	0.7 % <sup>3+2</sup>	1.9 % <sup>3</sup>
Module Part	Outer Wheel			Inner Wheel		
Compartment	Front	Middle	Back	Front	Middle	Back
Front	5-8 % <sup>2</sup>	0.2 % <sup>1</sup>	0.01 % <sup>4</sup>	-	-	-
Middle	0.2 % <sup>1</sup>	1.0 % <sup>2+3</sup>	1.0 % <sup>3+2</sup>	-	1.0 % <sup>2+3</sup>	0.5 % <sup>3+2</sup>
Back	0.2 % <sup>4</sup>	0.5 % <sup>3+2</sup>	3.0 % <sup>3</sup>	-	0.8 % <sup>3+2</sup>	2.0 % <sup>3</sup>

Table 3. *Summary of the typical cross talks measured in the different samplings of the barrel electrodes A and B and the outer and inner wheel of the endcap. The indices denote the nature of the cross talk where 1, 2, 3 and 4 correspond to resistive, capacitive, inductive and mixed respectively.*

mixture of various effects, but is mostly inductive. Since the back compartment plays an important role in the assessment of the longitudinal shower energy leakage it is important that this effect is measured and corrected for.

All these effects were expected and are well understood. They were measured on all modules. All cross talk effects are well reproducible among modules.

### 2.6.2 Treatment of Strips Capacitive Cross talk

Because an electron cluster contains a large number of strips (see Sec. 4.2 and Sec. 5.1.1) almost all the electron signal is contained in the cluster cells. Therefore any signal exported from one strip to its neighboring strips is recovered in the reconstructed cluster energy. The energy of an electron or photon cluster is therefore at first order not sensitive to the cross talk effect. However, the readout electronics are calibrated using pulse patterns where one strip cell is pulsed out of four. To recover the signal loss in the neighboring cells, the signal readout in the two first neighbor unpulsed cells is added to the pulsed cell and the average of the two next to nearest neighbor unpulsed cells are also added to the pulsed cell. In doing so using calibration runs where the signal is sampled in 32 time intervals of one nanosecond the shape of a signal in absence of cross talk is emulated. This new shape is used to derive the OF coefficients and comparing it to the signal shape without applying the summing procedure a correction factor of the ramp gains is derived. The amplitude of

the correction is around 7 %. The method has proven to be linear as the correction factors appear to be independent of the DAC signal applied. When the complete correction is applied, the  $M_{Phys}/M_{Cal}$  factor recovers a value of approximately 1 (its expected value if the signal reconstruction is sound) as illustrated in Fig. 5.

It was also checked that the method is not sensitive to gain differences between neighboring cells. To avoid the possible calibration differences between strip cells, the signal read in the non-pulsed cells is first calibrated and then added. However, no noticeable difference is seen between the two approaches.

Strip cells cross talk corrections show collective variations of approximately 1 % of the strips energy. The devised correction thus improves the uniformity of the energy measurement for the total electron energy of a few percent relative but has almost no impact on the local energy resolution.

### 2.6.3 Feedthrough Resistive Cross Talk

For all modules tested in the beamline the same two FT devices equipping the test beam cryostat were used. One unexpected and more tedious cross talk effect appeared in the bottom barrel modules FT which was lacking gold plated contacts. It exhibited an increase with time of the ground resistance common to all channels inside the connectors (64 channels), therefore a long range resistive cross-talk appeared. This problem non trivially affected most of the channels corresponding to that FT.

A correction procedure was derived which brought the uniformity of the response in channels readout with this feedthrough close to that of the other channels. However the data taken with the corrupted FT are not considered in the final analyses. These data correspond to electrons impinging at azimuthal angles  $\phi$  smaller than 9 in middle cell index units. To prevent this problem to appear in ATLAS, all connectors were gold plated and the connections were verified with the final detector.

## 3 BEAM TESTS EXPERIMENTAL PROTOCOLS

### 3.1 Beamline Setups

The barrel and endcap production modules have been exposed to beams at CERN with 245 GeV electrons in the H8 line and 120 GeV electrons in the H6 line respectively. The pion contamination of the electron beam was discussed

in [21], it is far less relevant in this context as a small bias would equally affect all the data. Similar pion contamination rejection cuts as those used in [21] were nevertheless used. Each experimental setup has been already described in details in [6] and [7]. Each beam line is instrumented with multi wire proportional chambers to extrapolate the particle impact on the calorimeter. The trigger is built from the coincidence of three scintillators on the beam line defining a maximal beam spot area of  $4 \text{ cm}^2$ . While for the barrel the projectivity of the beam is ensured in both directions by a proper movement of the cryostat, for the endcap the cryostat is moved along  $\eta$  but for the  $\phi$  rotation the calorimeter is moved inside the argon. In the endcap the amount of dead material upstream of the calorimeter is almost constant at all electron impact points and amounts to  $1.5 X_0$ . Thus it does not introduce any effect in the response uniformity of the calorimeter. In the barrel, however, the amount of dead material upstream continuously increases with  $\eta$ .

### 3.2 Scanning Procedure

Runs are taken with different positions of the moving table in such way that the complete module is exposed to the beam. The positions are chosen in order to center projectively each middle cell of the modules into the beam. For this reason the cell coverage is not completely uniform. In particular, less electrons are impinging on the edge of the cells than in the center. Results are therefore commonly presented in units of middle cells  $(\eta, \phi)$  indices. Exceptions are made for certain regions of the barrel calorimeter that have been scanned with a half middle cell granularity.

### 3.3 Temperature Stability

Argon temperatures were readout and recorded on the barrel setup: the temperature stability is better than  $10 \text{ mK}$ , but the absolute temperature differs from one module to another. A  $-2.0 \%$  correction of the mean energy per degree is taken into account in the analysis [27].

### 3.4 Data Sets

For all barrel modules runs of 10 000 events were recorded at each cell position.

Additional runs were taken in order to perform systematic studies such as cell-to-cell transitions, the electrode A to electrode B transition, and to study the impact of changing front-end and calibration boards in the front-end crates.

In the outer wheel of the EC modules only the region  $1.525 < |\eta| < 2.4$  and  $0.075 < \phi < 0.725$  (corresponding to  $6 \leq \eta_{\text{cell}} \leq 40$  and  $4 \leq \phi_{\text{cell}} \leq 29$ ) was covered. In the inner wheel the domain  $2.6 < |\eta| < 3.1$  and  $0.2 < \phi < 0.7$  (corresponding to  $45 \leq \eta_{\text{cell}} \leq 49$  and  $2 \leq \phi_{\text{cell}} \leq 6$ ) was covered representing 25 cells.

In the ECC0 and ECC1 modules high voltages were incorrectly cabled in the inner wheel. The inner wheel uniformity was therefore only studied on ECC5.

In all modules a few single isolated channels were defectuous or not responding at all. Most of them were due to the readout electronics setup and were thus found in all running period for EC and barrel modules. For those problematic channels for which the problem is intrinsic to the modules, the modules have been repaired for their future use in ATLAS. For instance in the EC outer wheel, four (one) electrode front connectors in ECC0 (ECC5) were not properly plugged on their summing board. The corresponding cells ( $\sim 20$ ) are excluded from the analysis. To avoid such problems in ATLAS, connections of all production modules have been checked by specific measurements.

Type	Barrel			endcap		
	M10	P13	P15	ECC0	ECC1	ECC5
Bad Strips	0	3	1	5	8	6
Bad Middle	2	0	0	3	1	1
Bad Calibration	2	2	0	0		
No data	2	1	15	-	-	-

Table 4. *Number of channels which present no physical signal, those where no data were taken and those where the calibration line was defectuous for all barrel modules in the FT0 region only and all end-cap modules.*

A problem which may appear in the future running of ATLAS is the impossibility to run some sectors at the nominal values of high voltage (HV). In the EC modules the electrodes of three HV sectors were powered on one side only because of HV problems that appeared at cold. In this case the energy of the corresponding cells is simply multiplied by a factor of  $\sim 2$ . The resulting energy resolution is degraded by  $\sim 20\%$  in these sectors and by  $\sim 40\%$  at the  $\phi$ -transition with a good sector. The impact on the response uniformity is negligible. The correction could be refined at the  $\phi$ -transition with a good sector. These cells are kept in the encap modules analysis.

For the barrel and endcap modules the scanned cells that are neighboring a middle defectuous channel or which are behind a bad strip are excluded from

Module	Barrel			EC Outer Wheel (IW)		
	M10	P13	P15	ECC0	ECC1	ECC5
Scanned	324	324	324	874	910	844 (25)
Kept	278	305	299	799	840	816 (25)
	86 %	94 %	92 %	91 %	92 %	97 % (100 %)

Table 5. *Number of scanned cells that are kept for the uniformity analysis. The excluded cells are related to problems that are specific to the beam test. The numbers indicated in parentheses correspond to cells of the inner wheel. In the barrel section the altogether 756 cells were scanned on each barrel modules comprising of the FT0 and FT-1 but only those pertaining to the FT0 are kept.*

the analysis. The same procedure is applied for problems in the calibration. When a back or a presampler cell is defectuous no specific treatment is applied.

The regions covered in endcap and barrel modules are detailed in Table 5. For the cells removed from the analysis, in the future a special treatment involving an energy correction could be applied.

## 4 BARREL UNIFORMITY

### 4.1 Monte Carlo Simulation

As was done in [21] a full Monte Carlo description of the shower development of electrons penetrating the electromagnetic calorimeter barrel module has been carried out with the GEANT simulation version 4.8 [32]. The intricate geometry of the accordion and the material of the calorimeter is thoroughly described. All the particles are followed in detail up to an interaction range of  $20\mu\text{m}$ . The photon-hadron interactions are also simulated.

The material within the volume of the cryostat is thoroughly simulated (lead, liquid argon, foam, cables, motherboards and G10) using our best knowledge of its geometrical distribution as described in [8].

The absorber thickness and gaps were set to their nominal values as reported in [6] and not to the measured ones. The material contraction in cold liquid argon was not taken into account either. The main consequence of these small inaccuracies essentially results in a absolute scale effect of a few per mil and does not affect the uniformity.

The material outside and in front of the calorimeter is described in detail accounting for the energy lost near and far from the calorimeter. The case where bremsstrahlung photons are not reconstructed in the calorimeter, because they have been produced far upstream of the impact point, is thus taken into account.

The material distribution of the test beam set-up is illustrated in Fig. 7. The distributions are presented as a function of the  $\eta$  and  $\phi$  direction separately and cumulatively for the material before and in the presampler, the material between the presampler and the first accordion compartment and the material in the accordion calorimeter. These distributions correspond to Monte Carlo samples simulated along the  $\eta$  and  $\phi$  directions with a granularity of one middle cell. Each point contains at least five hundred events. To further illustrate the material along the  $\phi$  direction scans at various fixed  $\eta$  values are performed. It appears that the total amount of material is rather uniform in the  $\phi$  direction.

Unlike in the ATLAS experiment, in the test beam setup only a small amount of material is located upstream of the calorimeter. It is therefore a unique opportunity to test the simulation of the calorimeter alone.

In particular, the material upstream has been tuned by varying the amount of liquid argon in front of the presampler that is not well known from the construction. This allowed to optimize the agreement of the Monte Carlo with the data in the presampler alone. As was the case in [21] the best agreement is found for a thickness of 2 cm.

The large capacitive cross talk between strips is not simulated. The cross talk effect between the middle and back compartments of the calorimeter is taken into account in the simulation.

## 4.2 Clustering

The electron energy is reconstructed by summing the calibrated cell energies deposited in the three calorimeter compartments and in the presampler. A cluster is built around the cell with the largest energy deposit in the middle compartment. The cluster size, expressed in number of cells in  $\Delta\eta_{cell} \times \Delta\phi_{cell}$  is  $3 \times 3$  throughout the barrel. This choice reflects a good compromise between noise and energy containment. The energies deposited in the corresponding  $2 \times 3$  back cells located behind the middle cells of the cluster are then added. In the front compartment of the barrel all 24 corresponding strip cells in front of the middle cluster are added. In  $\phi$ , the cluster contains 1 or 2 cells, depending on whether the shower develops near or far from the cell center. In the presampler the corresponding 3 cells in  $\eta$  within the two corresponding  $\phi$  positions are chosen to be part of the cluster.

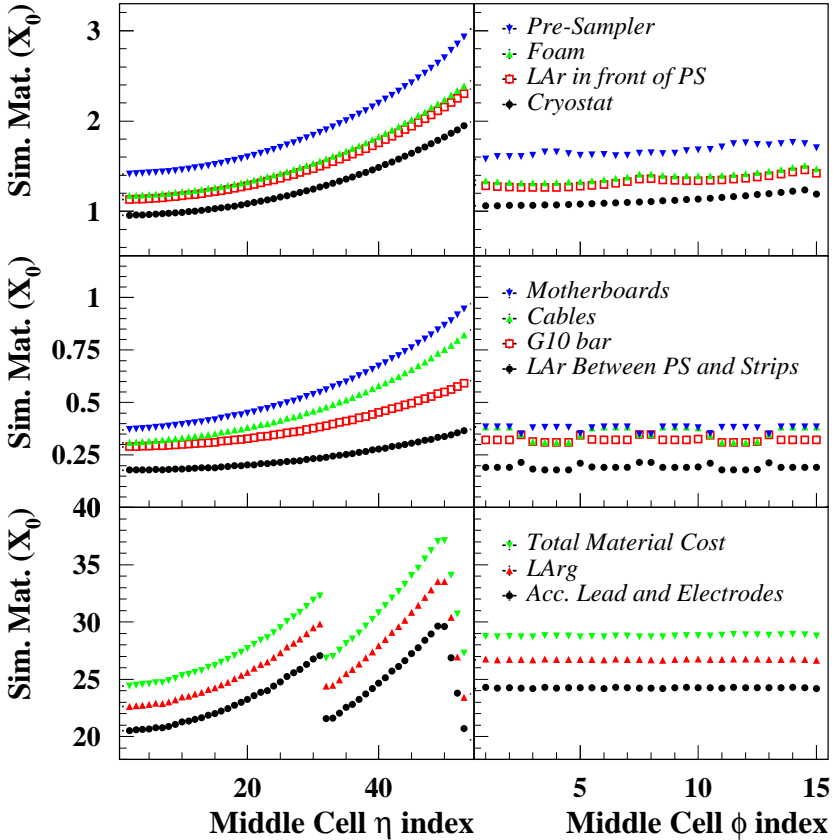


Fig. 7. *Distributions of the simulated material for the main material types in units of radiation lengths ( $X_0$ ) as a function of  $\eta$  and  $\phi$ . The upper two plots represent the cumulative amounts of material before and in the presampler. The two intermediate plots represent the cumulative distributions of the material between the presampler and the strips compartment of the accordion calorimeter. In order to illustrate the various structures in  $\phi$ , in the  $\eta$  plots the average values correspond to various fixed  $\phi$  values, the corresponding averages are thus different in  $\eta$  and  $\phi$ . The bottom two plots represent the amount of material in the accordion calorimeter as well as the total amount of material in the entire setup.*

#### 4.3 Energy Reconstruction Scheme

Several electron energy reconstruction schemes were tried. In particular the two most effective ones were those used in [21] and an additional reconstruction scheme which took into account the shower depth dependence of the sampling fractions and the leakage energy [33]. The energy reconstruction scheme used in [21] was chosen for its simplicity as it could be applied across the entire  $\eta$  range with a simple analytical parametrization. This energy reconstruction scheme is mostly based on our best knowledge of the detector as

implemented in the Monte Carlo simulation. The total reconstructed electromagnetic (EM) shower energy  $E_{rec}$  is evaluated from the measurements of the visible cell energies in the presampler ( $E_{PS}^{meas} = \sum_{PS} E_{vis}^{cell}$ ), all compartments of the accordion added together ( $E_{Acc}^{meas} = \sum_{Acc} E_{vis}^{cell}$ ), the energy measured in the strips ( $E_{Strips}^{meas} = \sum_{Strips} E_{vis}^{cell}$ ) and the energy measured in the back compartment ( $E_{Back}^{meas} = \sum_{Back} E_{vis}^{cell}$ ). These measurements are carried out within the EM cluster.

The basic principles of the energy scheme for the reconstruction of test beam electrons are reviewed in [21]. The total deposited energy is reconstructed in four steps: (1) the energy upstream of the presampler is evaluated using the measured presampler energy; (2) the energy deposited between the presampler and the strips is evaluated using the measured presampler and strips energies; (3) the energy deposited in the accordion is evaluated using the measured energy in the accordion cells; (4) the leakage energy is evaluated from the average expected leakage at a given position in the detector and the amount of energy in the last accordion compartment. The scheme can be written as follows:

$$E_{raw}^{rec} = a_\eta + b_\eta \times E_{PS}^{meas} + c_\eta \times \sqrt{E_{PS}^{meas} E_{Strips}^{meas}} + \frac{E_{Acc}^{meas}}{d_{eta}} + \xi(E_{Back}^{meas}) \quad (5)$$

yielding the raw reconstructed energy, corresponding to the complete raw shower energy.

As shown in Section 4.1, the amount of material is rather uniform in the azimuthal direction, therefore all parameters are derived only as a function of the  $\eta$  direction where the variations of material are large.

As explained in detail in [21], this energy scheme has numerous advantages with respect to the one used before [6]. The most prominent are:

- (i) It optimizes both resolution and linearity.
- (ii) The parametrization of the energy deposited between the presampler and the strips compartment of the accordion allows to sample a different part of the shower and to absorb most of the shower depth dependence of the overall sampling fraction.
- (iii) The offset in the parametrization of the energy deposited before the presampler allows to account optimally for the energy loss by ionization by the beam electrons.

The main differences with the energy scheme used in [21] are the following:

- (i) The parameters are derived as a function of  $\eta$  and not as a function of the energy as the scan is done at fixed energy.
- (ii) The leakage energy is derived from the energy in the back compartment

of the accordion. The electron energies in the present analysis are higher than those used in [21] where beam test runs were taken at a fixed  $\eta$  value of 0.687 corresponding to a region of the detector where the longitudinal leakage is the close to smallest. The expected leakage is much larger here. It has to be thoroughly corrected in order to reach a good energy resolution.

#### 4.3.1 Parametrization of the Calibration Parameters

The parameters of the shower energy reconstruction are derived for all positions in  $\eta$  in steps with the granularity of one middle cell. The parameters are derived by fitting the energies measured within the cluster with respect to the energies within the complete physical volume of the setup. This allows to take automatically into account a rather large lateral leakage typically amounting to  $\sim 5\%$  of the shower energy outside the cluster volume. The parameters of Eq. 5 found are displayed as a function of the middle cell  $\eta$  indices in Fig. 8. These parameters are obtained as follows.

- $a_\eta$  and  $b_\eta$ : are fitted using the distribution of total energy deposited prior and in the presampler versus the energy measured in the presampler within the cluster. As expected, the offset  $a_\eta$  scales with the amount of material and the sampling  $b_\eta$  parameter is almost constant.
- $c_\eta$ : is fitted using the distribution of total energy deposited between the presampler and the strips compartment of the accordion versus the square root of the product of energy measured in the presampler and the strips (corresponding to the geometrical average of these two energies).
- $d_\eta$ : is fitted using the distribution of the total energy deposited in the accordion versus the measured energy in all compartments of the accordion within the electromagnetic EM cluster.

The discontinuity in the parameters  $c_\eta$  and  $d_\eta$  is due to the difference in lead thickness between the electrodes A and B. Apart from the discontinuity at the transition, the accordion total sampling fraction is mostly constant.

The variation of the  $c_\eta$  parameter reflects the non trivial interplay of two effects: the design of the strips was made with a constant longitudinal extent in units of radiation lengths corresponding to about  $4X_0$  and the design of the presampler which has a constant thickness and thus has an increasing depth in units of radiation lengths.

#### 4.3.2 Longitudinal Leakage Energy Parametrization

Depending on the  $\eta$  coordinate of electrons impinging at 245 GeV on the modules the amount of leakage can reach non negligible values. However, these amounts are rather small in regions far from the edges of the modules. A simple

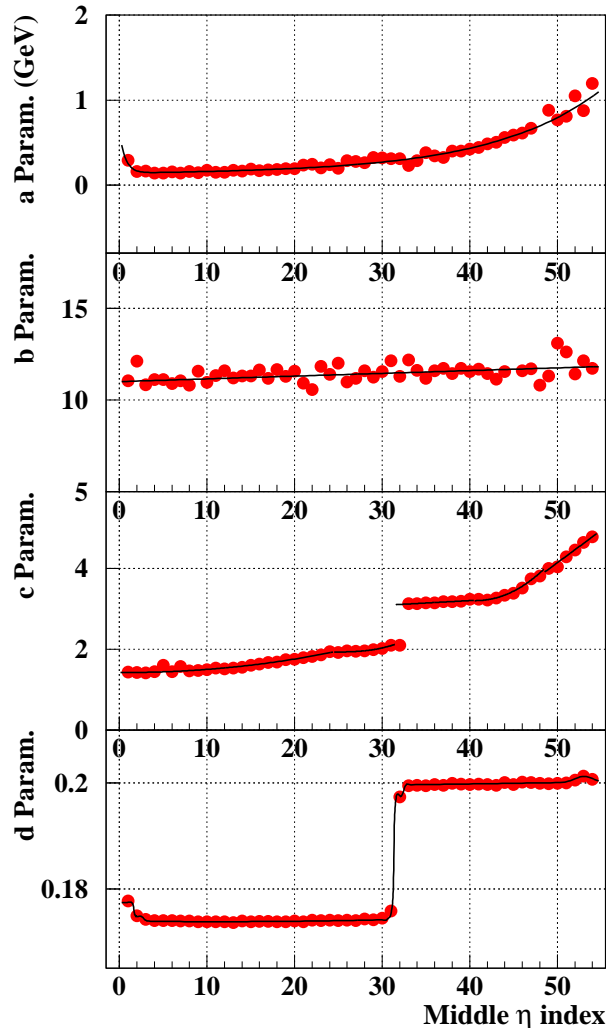


Fig. 8. Calibration parameters used to reconstruct the cluster energy. In the first and second upper figures the constant and linear coefficients respectively of the parametrization of the energy deposited before and within the presampler are shown. In the second lowest figure the parameters of the energy reconstruction between the strips and the presampler are illustrated. The last figure represents the accordion sampling fraction. The functional parametrization of all the parameters is also shown.

correction corresponding to adding the average value of the expected leakage energy as a function of the location of point of impact would be sufficient in regions where the average leakage does not exceed a few GeV. However, in order to optimize the energy resolution in the regions near the module edges, the correlation between the energy deposited in the back compartment of the accordion and the energy lost longitudinally can be exploited. The correlation between the longitudinal leakage energy and the energy deposited in the Back

compartment of the accordion is shown in Fig. 9 where the leakage energy is represented as the difference between the leakage and its average value for a given pseudo rapidity. The average leakage is shown in the upper plot of Fig. 10.

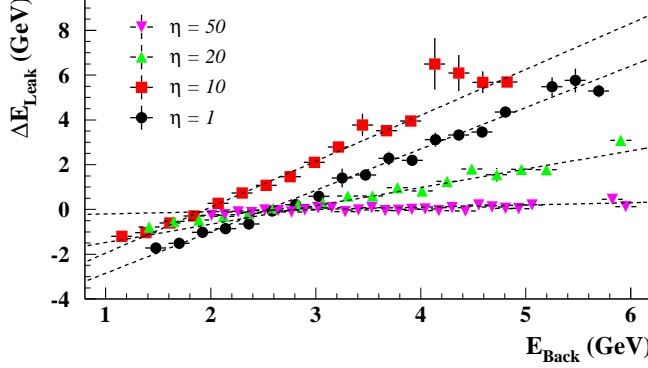


Fig. 9. *Difference between actual and average leakage energy as a function of the energy deposition in the back compartment for various electron impact points.*

The average values of the longitudinal leakage are parametrized as a function of the pseudo rapidity of the impact position of the electron, as measured by the strips. The expected distributions of the energy leakage as a function of the energy measured in the back compartment are fitted for all pseudo rapidities with a granularity of one middle accordion cell as follows:

$$\Delta E_{\text{Leak}}(\eta) = E_{\text{Leak}}(\eta) - \langle E_{\text{Leak}} \rangle(\eta) = \alpha_\eta + \beta_\eta E_{\text{Back}}(\eta)$$

The  $\beta_\eta$  factor represents the approximately constant ratio of energy leaked longitudinally and the energy deposited in the back compartment. The  $\alpha_\eta$  term can be interpreted as the weighted average energy in the back compartment *i.e.*  $\alpha_\eta = -\beta_\eta \langle E_{\text{Back}} \rangle$ .

The results of these fits are also parametrized as functions of the pseudo rapidity. The leakage is assessed analytically as follows:

$$\xi(E_{\text{Back}}^{\text{meas}}) = \langle E_{\text{Leak}} \rangle(\eta) + \alpha_\eta + \beta_\eta E_{\text{Back}}(\eta)$$

It is then simply added to the shower energy to form the raw reconstructed energy.

In this procedure the leakage energy depends largely on the energy deposited in the back compartment of the calorimeter. Since the leakage correction is evaluated from the Monte Carlo, it is crucial that the cross talk between middle and back as described in Section 2.6 be well understood. Because all

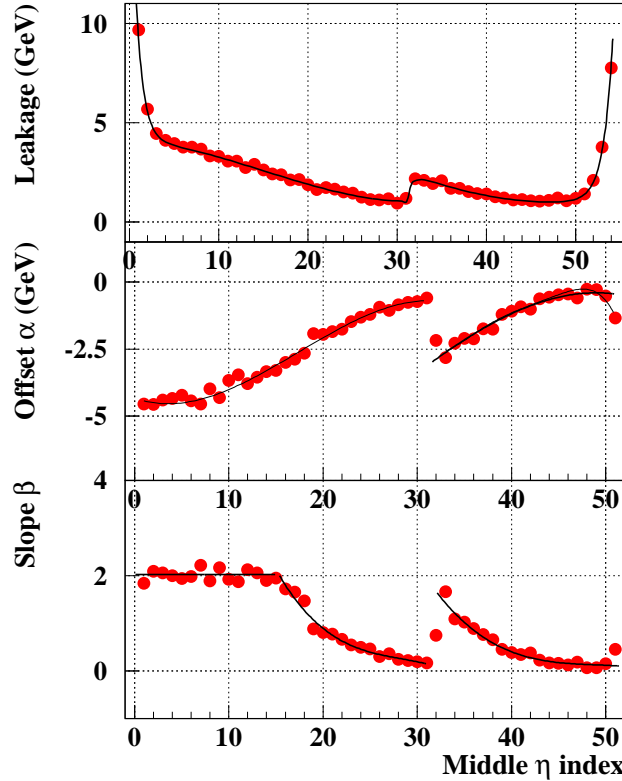


Fig. 10. *Calibration parameters used to reconstruct the leakage energy. The upper plot illustrates the average leakage energy as a function of pseudo rapidity. The second and third plots show the variations in  $\eta$  of the constant ( $\alpha$ ) and linear ( $\beta$ ) coefficients used to reconstruct the leakage energy on an event-by-event basis using the measured energy in the back compartment.*

measured values of this effect are compatible, it is corrected for in the Monte Carlo. The leakage correction can then be directly applied to the data.

The linear correlation between energy deposition in the back compartment and the leakage energy is manifest. However, at low values of energy deposition in the back compartment the leakage energy is systematically above that expected from a pure linear correlation. This effect arises from events where an early hard hadronic photon-nucleus interaction occurs within the showering process. The produced hadronic particles escape the volume of the electromagnetic calorimeter implying a large longitudinal leakage without depositing any significant amount of energy in the back compartment. Such events are relatively rare but when they occur they carry a lot of energy outside the calorimeter. In this analysis those events presenting a very large leakage due to photon-nucleus interaction are removed by the pion hadronic veto. The events with a small though non negligible fraction of leakage from a photon-nucleus interaction could not be properly treated in our test beam protocol.

Nevertheless a correction could be designed for ATLAS where the hadron calorimeter could catch the hadronic tails of electrons undergoing hadronic interactions.

#### 4.4 Energy Reconstruction Scheme Performance

The application of the described energy reconstruction scheme to the Monte Carlo simulation for electrons impinging a single cell of the middle compartment results in a non-uniformity of 0.10 %. The uncertainty due to limited statistics of the Monte Carlo samples implies a non uniformity of about 0.05 %. The expected systematic non uniformity arising from the Monte Carlo parametrization thus amounts to 0.09 %.

#### 4.5 Comparison of Data to Monte Carlo

As mentioned in Sec. 2.4.3, the conversion factor  $f_{I/E}$  from current to energy is estimated from a comparison of data and the Monte Carlo simulation. The presampler and the accordion are normalized independently for each electrodes A and B. For the 2001 running period the normalizations are evaluated from a comparison between M10 data and the Monte Carlo simulation. For the 2002 running period the normalization is estimated using the P13 data only. The constants derived from the comparison with the module P13 are also applied to the P15 module. When comparing the ratio of the constants derived from the data between electrodes A and B to those directly inferred from first principles, as described in Sec. 2.4.3, in the simulation the difference amounts to less than 1 %.

To illustrate the performance of the simulation Fig. 11 displays a comparison of the visible energy in the data of the module P15 with the Monte Carlo for each individual compartments of the calorimeter as a function of the  $\eta$  middle cell index. A general very good agreement is observed. In particular, it can be noted that:

- (i) The overall energy calibration of the module P15 is in good agreement with that of the module P13 and moreover the inter-calibration of the electrodes A and B is also well reproduced.
- (ii) The good agreement in the absolute scale of the strips results from a sound treatment of the large capacitive cross talk.
- (iii) The overall acceptable agreement in the back compartment illustrates that cross talk between the middle and back compartments has been correctly taken into account.

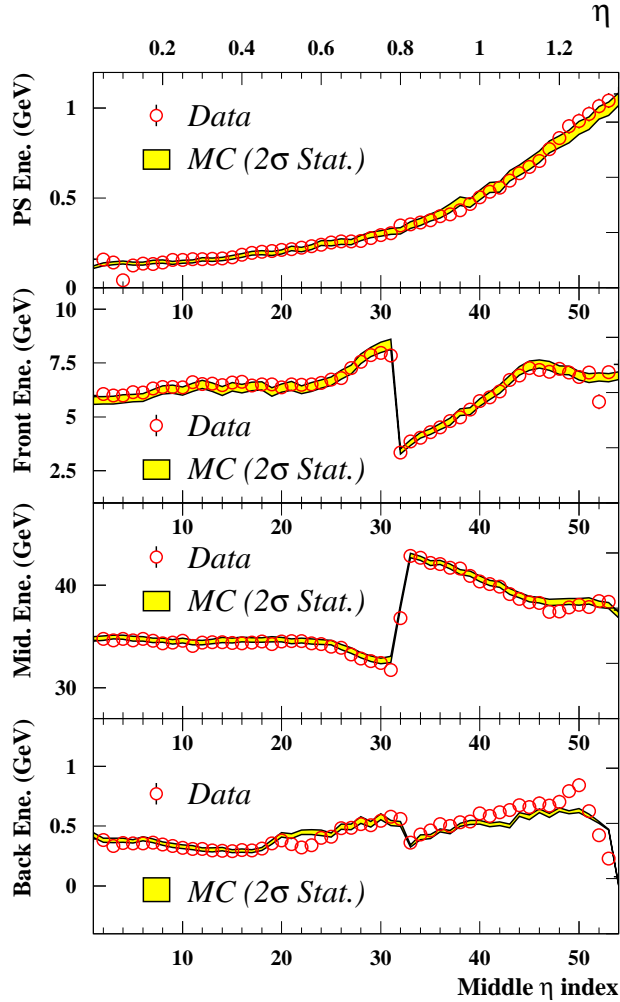


Fig. 11. *P15 data versus Monte Carlo comparison in the  $\eta$  direction for each compartment individually: the presampler (PS); strips (front), Middle (Mid.) and Back. The comparison is made at the constant  $\phi$  middle cell index of 11.*

#### 4.6 Cluster Level Corrections

To improve the accuracy of the energy reconstruction there are three further effects that should be taken into account. The first one is the cluster energy dependence on the EM particle impact position within one middle cell. Along the  $\eta$  and  $\phi$  directions although the transverse leakage is corrected for there is a residual energy modulation effect due to the limited extent of the cluster. Along the  $\phi$  direction there is an additional energy modulation due to the structure of the interleaved accordion absorbers. These two effects are taken into account in the correction factor  $f_{CI}(\eta, \phi)$ . The second effect is the energy loss in the electrodes transition region. It is corrected using the factor  $f_{TR}(\eta)$ . The third effect is the systematic variation in the electronic calibration due to

differences in calibration cable lengths. It is corrected by means of the factor  $f_{Cables}(\eta)$ . The final EM particle energy reconstruction scheme can be written as follows:

$$E^{rec} = (E_{raw}^{rec} \times f_{CI}(\eta, \phi) \times f_{TR}(\eta) \times f_{Cables}(\eta))$$

#### 4.6.1 Energy Modulation Corrections

In order to correct for the energy modulations using data, a precise and unbiased measurement of the impinging electron impact position is necessary. The  $\eta$  position is accurately given by the energy deposition in the strips. A simple weighted average yields an accurate estimation of the pseudo rapidity of the electron impact on the calorimeter. In the azimuthal direction the finest granularity is given by middle cells and is eight times coarser than that of strips along the  $\eta$  direction. Given the exponentially slender electron shower profile the azimuthal coordinate given by the weighted average of the energy depositions in the middle compartment is biased towards the center of the cell. This bias is referred to as S-shape alluding to the shape of the distribution of the reconstructed position with respect to the original one. It is also present along the  $\eta$  direction but can be neglected in these studies. Advantage is therefore taken of the precise position measurement of the wire chambers located in the test beam to evaluate this S-shape in order to re-establish an unbiased estimate of the azimuthal coordinate of the cluster. An energy distribution as a function of  $\eta$  and  $\phi$  is evaluated for each middle cell of the P13 module. These distributions correspond to sliding averages of five cells in  $\eta$  in order to accumulate enough statistics to precisely fit the shape of the modulations. All cells are fitted and the evolution of the fit coefficients are parametrized. The modulation correction is therefore fully analytical. All spectra in  $\eta$  and  $\phi$  are displayed in Fig. 12 and grouped into four regions in  $\eta$ .

The energy modulations in  $\eta$  are parametrized by a parabola as follows:

$$E_{\eta-corr.}(\eta) = E_{raw}^{rec} / \left[ 1 + C_1(\eta - \eta_C) + C_2(\eta - \eta_C)^2 \right] \quad (6)$$

where  $E^{rec}$  is the raw electron reconstructed energy,  $\eta_C$  is the coordinate of the maximum of the parabola.  $C_2$  is the curvature of the parabola. It is directly linked to the amount of lateral leakage.  $C_1$  is a linear term that introduces an asymmetry in the energy distribution as a function of  $\eta$ . This asymmetry is expected given the cells geometry. The latter term is always very small. All coefficients are then parametrized using simple functional forms throughout the module.

When the aforementioned S-shape correction is applied, the energy modula-

tions become consistent with an expected two-fold modulation with lengths in middle cell units of 1/4 and 1/8 folded with a parabola resulting from the finite size of the cluster. As shown in Fig. 12 all modulations in the barrel are observed and they display common features. The energy is thus corrected in the following way:

$$E_{\phi-corr.}(\phi_{abs}) = E_{raw}^{rec}/[(1 + C_1(\phi_{abs} - \phi_C) + C_2(\phi_{abs} - \phi_C)^2) \times a_{8\pi}(\cos 8\pi(\phi_{abs} - \phi_C) + a_{16\pi}(\cos 16\pi(\phi_{abs} - \phi_C))]$$

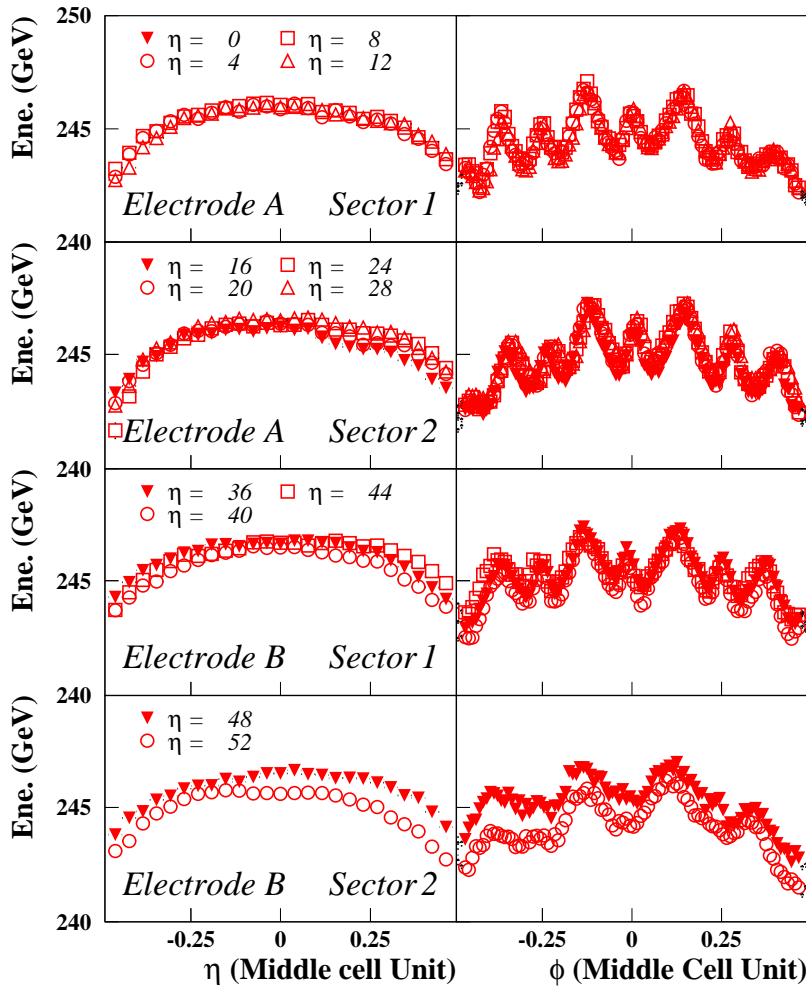


Fig. 12. Energy modulations as a function of the  $\eta$  (left plots) and  $\phi$  (right plots) directions for different regions covering middle cell indices in the  $\eta$  direction and integrating four cells units both in the azimuthal and pseudo rapidity directions.

$\phi_C$  is the azimuthal coordinate of parabola's maximum. The coefficients  $C_1$  and  $C_2$  are the parameters of the parabola. The linear term is again negligible.

$a_{8\pi}$  and  $a_{16\pi}$  are the amplitudes of the 1/4 and 1/8 modulations respectively. All coefficients are also parametrized using simple functional forms throughout the module.

As can be seen in Fig. 12 the modulations are less pronounced in the cells placed at larger pseudo rapidities. This effect is likely due to the mechanical positioning of the module in the test beam. A slight deviation from a projective beam impact on the module can produce such an effect.

When the modulation corrections are applied, an improvement in the overall energy resolution of typically 30 % is observed.

#### 4.6.2 Lead transition reconstruction

Due to the cylindrical geometry of the barrel calorimeter the sampling frequency decreases with pseudo rapidity. In order to balance the energy resolution each module consists of two parts with two separate electrodes and different lead thicknesses. The lead thickness at high pseudo rapidity is smaller in order to increase the sampling fraction and the sampling frequency, given that the geometry is unchanged. Unfortunately the transition between the electrode A at low pseudo rapidity and electrode B at higher pseudo rapidities involves a small uninstrumented region of roughly 2-3 mm.

In order to study in detail this transition, special high statistics runs were taken with the P13 module with electrons uniformly covering the transition region. The average energy evaluated from a Gaussian fit to the fully corrected energy distribution in  $\eta$ -bins of a quarter of one strip cell unit as a function of the pseudo rapidity is shown in Fig. 13. Due to the discontinuity in the lead thickness the sampling fractions are also discontinuous, therefore in order to have a continuous energy distribution across the transition, electron sampling fractions need to be applied at the cell level.

At the transition, the electron energy measurement can be underestimated by up to  $\sim 20$  %. The width of the energy gap is approximately three strip cells large. A double Fermi-Dirac function added to a Gaussian is used to fit the energy loss as shown in Fig. 13. In this figure the deterioration factor ( $\sigma_T/\sigma_S$ , where  $\sigma_T$  and  $\sigma_S$  are the resolutions at the transition and in the neighboring middle cells) in energy resolution is also shown. After the correction is applied, the energy resolution is degraded by a factor  $\sim 2$  over a range of three strip cells units. However the region where the energy resolution is deteriorated is very small and corresponds to approximately 0.003 ( $\sim 1$  strip cell) in units of pseudo rapidity.

The asymmetry in the loss of energy is due to the increase in bending angle with depth to maintain a constant gap. The electrodes were designed to ac-

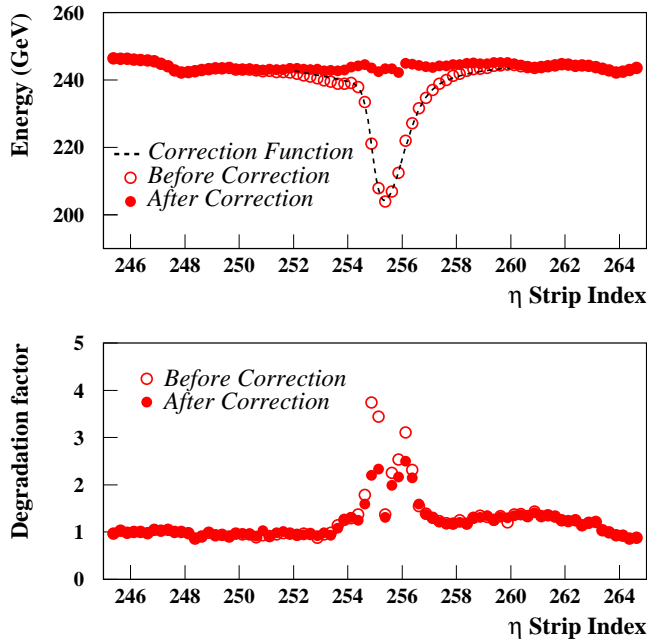


Fig. 13. In the upper figure the variations of the measured energy across the transition gap between electrodes A and B before and after the correction is applied are illustrated. The functional form used to correct for the energy loss in the transition is also shown. The lower plot illustrates the degradation of the energy resolution with respect to the neighboring cells throughout the transition.

count for this effect and the gap distortion was unfolded in the pre-bending design. That was not the case for the absorbers which present a curved transition after bending. In the Monte Carlo this effect was taken into account and the gap width was tuned to 2.5 mm on the data. This value corresponds precisely to the one measured on the modules.

#### 4.6.3 Cable Length Correction

The calibration cables carrying the signal from the calibration boards to the motherboards have different lengths. The resulting variation in the input signal attenuation is corrected for with the factor  $f_{Cables}(\eta)$  which is evaluated from detailed measurements of the cable lengths. Because the attenuation occurs before the calibration signal injection it introduces a small bias in the calibration procedure. The correction is made *a posteriori* at the cluster level in each layer. It amounts to  $\sim 1.5\%$  in average and its variations with pseudo rapidity are small (of the order of one per mil).

## 4.7 Modules Uniformity

When all corrections are applied the energy distribution for each run corresponding to one middle cell unit for all barrel modules is fitted with a Gaussian form starting from  $-1.5\sigma$  off the mean value to determine both the average energy and resolution. All problematic cells described in Sec. 4.2 are excluded. The mean energies resulting from the fits to the energy distribution corresponding to the FT0 of all barrel modules as a function of  $\eta$  and for all  $\phi$  values are shown in Fig. 14.

Module	$\eta$ Range		
	Overall [1-54]	Electrode A [1-31]	Electrode B [32-54]
M10	$0.48 \pm 0.03 \%$	$0.48 \pm 0.03 \%$	$0.45 \pm 0.03 \%$
P13	$0.43 \pm 0.03 \%$	$0.35 \pm 0.03 \%$	$0.48 \pm 0.03 \%$
P15	$0.40 \pm 0.03 \%$	$0.36 \pm 0.03 \%$	$0.43 \pm 0.03 \%$

Table 6. *Non-uniformity expressed in terms of RMS values of the dispersion of the average energies in the FT0 domain, overall and for each electrode A and B independently. The statistical uncertainties are also displayed.*

A measure of the non-uniformity at the granularity level of one middle cell is given by the dispersion (RMS/ $\langle E \rangle$ ) of the measured averages. The values obtained are summarized in Table 6.

Non uniformities of the calorimeter response are typically of the order of one half percent.

The widths of the aforementioned Gaussian energy fits as a function of  $\eta$  and for all values of  $\phi$  pertaining to the FT0 are shown in Fig. 15. As can be seen in Fig. 15 in module M10 around the middle cell  $\eta$  index of 14 and in the modules P13 and P15 around the index 48, a degradation of the resolution is observed. These effects are due to bad presampler cells. An overall better energy resolution is obtained in the module P15, although the modulation corrections were derived from the module P13. The origin of this difference cannot be easily traced back. Matter effects could be responsible for differences in local energy resolution between the module P13 and P15 either at the level of the constant term or due to differences in the stochastic term. Differences in manufacturing quality could produce such an effect.

The general increasing trend of the resolution with respect to pseudo rapidity is in part due to the increase of the stochastic term and in part due to the increase of material upstream.

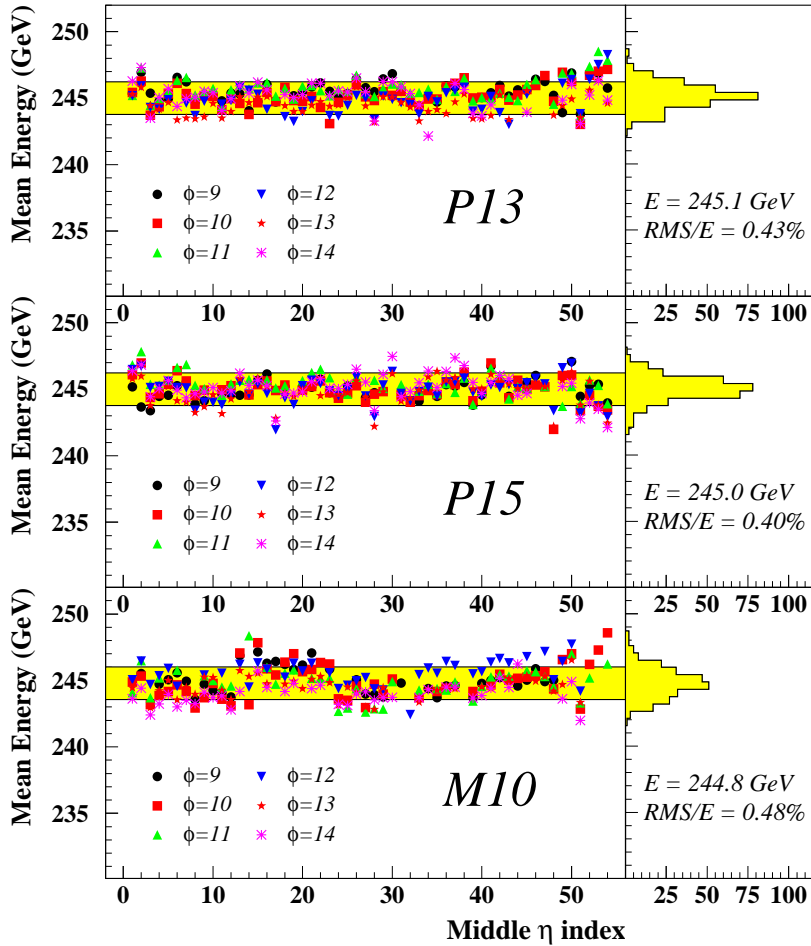


Fig. 14. Summary of the energy measurements for each barrel module for all cells of the FTO as function of pseudo rapidity. The overall distribution is shown and the corresponding average and dispersion values are indicated. The bands corresponds to twice the dispersion of the measurements.

As expected, at the electrode transition where the absorber thickness changes, a discontinuity in the energy resolution is observed.

#### 4.8 Relative Energy Scale

The P13 and P15 modules were exposed to the test beam with the same calibration and readout electronics and with the same upstream material. The absolute energy scales for these modules should therefore be very close or it could imply that a problem at the construction level occurred. The average reconstructed energy values for the P13 and P15 modules are  $245.1 \pm 0.06 \text{ GeV}$  and  $245.0 \pm 0.05 \text{ GeV}$ , respectively corresponding to a relative difference of

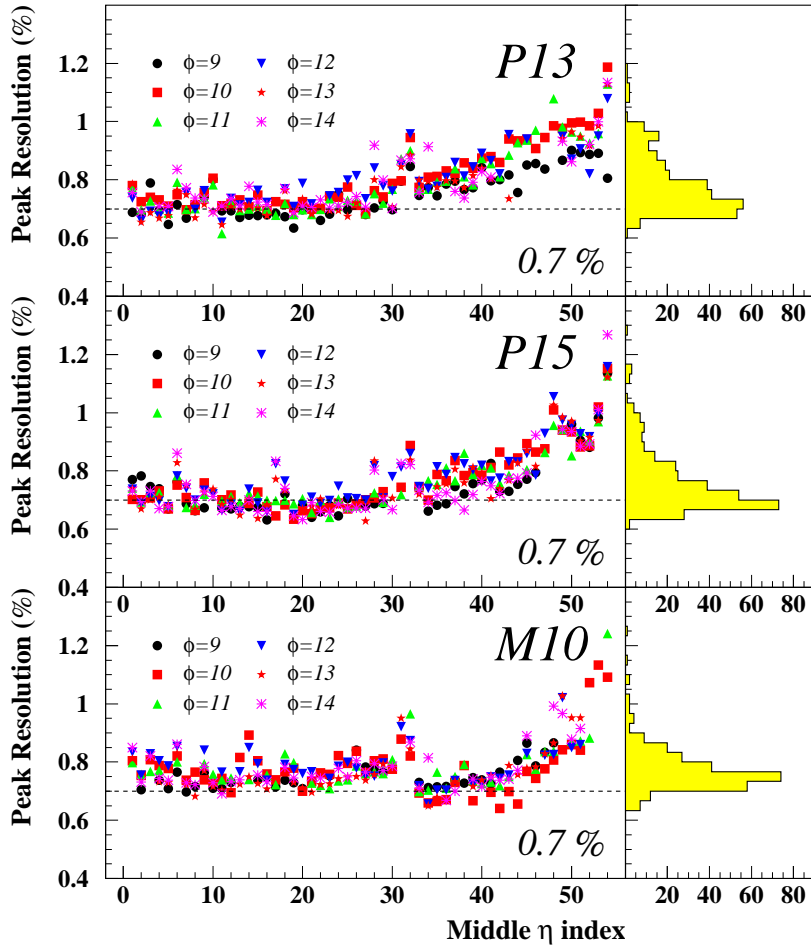


Fig. 15. *The local resolution of the cell energy measurements for all modules and all cells as a function of pseudo rapidity.*

less than 0.1 %. This global non-uniformity contribution to the overall energy resolution is small compared to the non-uniformities observed within each module.

#### 4.9 Uncorrelated Non Uniformities

In order to disentangle the correlated non uniformities from the uncorrelated ones, for each cell of the scan the ratio of the average energies is computed. The distributions plotted in Fig. 16 are averages in  $\phi$  and in  $\eta$  of the mean energy in each cell and their ratio. The uniformity of the ratio corresponds to the combination of the non correlated uniformities of the two modules. The dispersion of the distribution of the ratios amounts to 0.30 %. The variations in azimuthal angle are small as shown in Fig. 16.

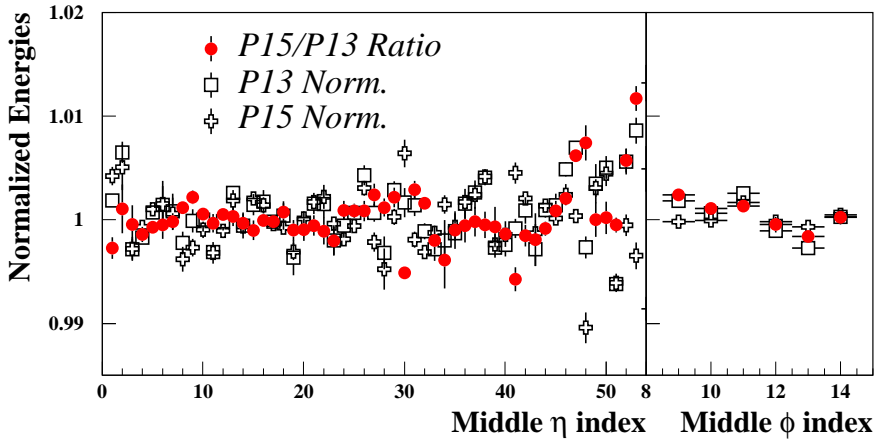


Fig. 16. *Profiles of the normalized energy distributions as a function of pseudo rapidity and azimuthal angle for the modules P13 and P15 and their ratio. These profiles are obtained by averaging over the FT0 cells in  $\phi$ .*

#### 4.10 Correlated Non Uniformities

Correlated non uniformities are typically due to the reconstruction method, inaccuracies in the Monte Carlo simulation or inaccuracies in the energy corrections. Since the P13 and P15 modules used the same front-end and calibration electronics their related non-uniformities are accounted for as correlated.

Module	Section	Total	Correlated	Non Correlated
P13	Overall	0.43 %	0.34 %	0.26 %
	Electrode A	0.35 %	0.29 %	0.20 %
	Electrode B	0.48 %	0.34 %	0.34 %
P15	Overall	0.40 %	0.34 %	0.21 %
	Electrode A	0.36 %	0.29 %	0.21 %
	Electrode B	0.43 %	0.34 %	0.26 %

Table 7. *Details of the correlated and non correlated non-uniformities for the P13 and P15 modules. The values corresponding to the electrode A and B are also given separately.*

Using the dispersion of the ratio of the measured energies for the modules P13 and P15, the correlated and the uncorrelated contributions to the uniformity can be separated. The values of correlated and non correlated non uniformities are displayed in Table 7.

## 4.11 Contribution to the Non Uniformity

All contributions to the non uniformities of the calorimeter response cannot be easily disentangled. Merging the beam test results with the quality control measurements, the electronics performance evaluation and the monte carlo simulation, a non exhaustive list of sources of non uniformity, displaying the most prominent contributions, is proposed hereafter.

### 4.11.1 *Electronics Calibration System*

The calibration system was built within very strict requirements regarding the precision of the electronics components. The entire system was thoroughly reviewed and tested. The precision of the three possible sources of non uniformity (pulsers, injection resistors and cables) was estimated. All calibration boards were measured on a test bench and were found to fulfill the requirements. Non uniformities arising from the calibration system are detailed in 2.3 and displayed in Table 8. The overall non uniformities amounts to  $\sim 0.23\%$ . This estimate is mostly correlated between the modules P13 and P15.

### 4.11.2 *Readout Electronics*

Assuming that the calibration system is uniform, the properly calibrated readout electronics should not contribute to non-uniformities. However, small differences in the readout response could infer second order effects that could imply variations in the calorimeter response. In order to assess these variations, data was taken with the P15 module where two middle cells Front End Boards (FEB) were permuted. The new FEB configuration was calibrated and new data were taken. The variation in the energy measurement with the board swap amounted to approximatively 0.1 %.

### 4.11.3 *Signal Reconstruction*

For various runs taken on the P15 module the data were reconstructed using the two methods described in Sec. 2.5. In order to assess the possible non uniformities arising from the signal reconstruction method the dispersion of the differences in the average energy between the two methods is taken. The observed RMS amounts to 0.25 %. This estimate is likely to be an overestimate of the intrinsic bias of the method.

#### 4.11.4 Monte Carlo Simulation

The full Monte Carlo simulation of the experimental setup cannot perfectly reproduce the actual data. Non uniformities in the calorimeter response can thus arise from the simulation. The precision of the Monte Carlo description will directly impact the energy measurement. The difference between data and Monte Carlo presented in Sec. 4.5 amounts to 0.08 %. This figure, derived from the dispersion of the distribution of the difference in measured energies between data and Monte Carlo, represents the expected non uniformity arising from the simulation inaccuracies.

#### 4.11.5 Energy reconstruction Scheme

The energy reconstruction scheme involves a large number of parameterizations and fits. Inaccuracies of these parameterizations will impact the energy measurements and can induce a non uniform response. A measure of the inaccuracies of the parametrization is the residual systematic non uniformity in the Monte Carlo simulation. As was shown in Sec. 4.4, this effect amounts to 0.09 %.

#### 4.11.6 Module Construction

The non uniformities related to the construction of the modules are the dominant source of non-correlated non uniformities. The main sources of the non-uniformity in the construction of modules are the lead thickness and the gap dispersion.

- (i) The impact of the variations in lead thickness on the EM energy measurements was assessed and a scaling factor of 0.6 was found between the dispersion of the lead thickness and the dispersion of the EM energies.
- (ii) Similarly the impact of the variations of the gap were studied and a scaling factor of 0.4 was found between the dispersion of the gaps and that of the EM energy measurements.

From the measurements presented in Sec. 1.4.1 the expected non uniformity obtained are displayed in Table 8.

#### 4.11.7 Modulation Corrections

The energy modulation corrections can impact the calorimeter response to electrons at different levels either by affecting the uniformity or the local constant term.

The modulation corrections were evaluated on the module P13 only and were then applied to all other modules. For this reason it is difficult to disentangle the correlated from the non correlated part of the correction. For the sake of simplicity this effect will be considered as exclusively non correlated. To evaluate its impact both on the uniformity and on the local constant term, the complete analysis is done restricting the measurement to a small region accounting for 20 % of the cell around its center. The differences found are of 0.14 % and 0.10 % for the modules P13 and P15 respectively.

#### 4.11.8 Time Stability

In order to check the stability of the energy reconstruction, reference cells were periodically scanned with the 245 GeV electron beam. Two cells were chosen for the modules P13 and P15 both at a middle cell  $\phi$  index of 10 and at  $\eta$  indices of 12 and 36. For the module M10 only one reference cell was taken at an  $\eta$  index of 34. The variation of the energy reconstruction with time is illustrated in Fig. 17.

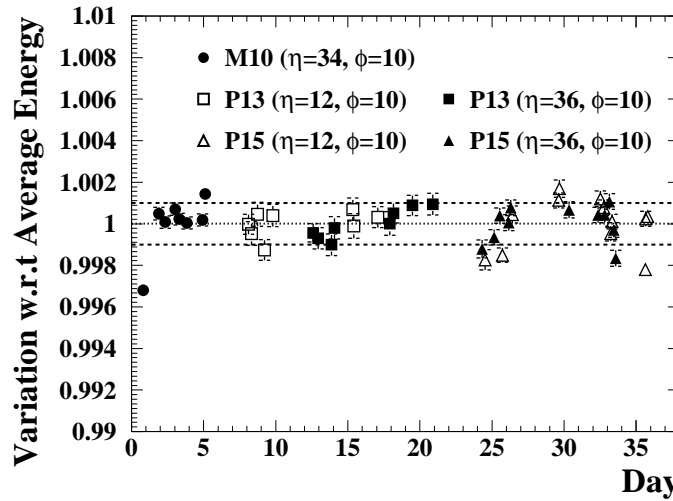


Fig. 17. Energy measurements for two reference cells in modules P13 and P15 and in module M10, as a function of time. The  $\pm 10\%$  variation band is also indicated.

From the observed variations, the impact on the energy measurements are estimated to be 0.09 %, 0.15 % and 0.16 % for the modules P13, P15 and M10 respectively.

#### 4.11.9 Summary

All known contributions to the non uniformity are summarized in Table 8. The good agreement achieved between the data and the expectation illustrates that

the most sizable contributions to the non uniformities have been identified.

Correlated Contributions	Impact on Uniformity	
Calibration	0.23 %	
Readout Electronics	0.10 %	
Signal Reconstruction	0.25 %	
Monte Carlo	0.08 %	
Energy Scheme	0.09 %	
Overall ( <b>data</b> )	0.38 % ( <b>0.34 %</b> )	
Uncorrelated Contribution	P13	P15
Lead Thickness	0.09 %	0.14 %
Gap dispersion	0.18 %	0.12 %
Energy Modulation	0.14 %	0.10 %
Time Stability	0.09 %	0.15 %
Overall ( <b>data</b> )	0.26 % ( <b>0.26 %</b> )	0.25 % ( <b>0.23 %</b> )

Table 8. *Detail of the expected contributions to the uniformity and to the constant term.*

The module P15 displays a slightly better uniformity than the other modules. None of the control measurements support this observation. However, as shown in Sec. 1.4.1 the granularity of the control measurements was not particularly high. Manufacturing differences within such granularity may not be observable but could impact the uniformity.

#### 4.12 Local and Overall Constant Term

The distributions of all energy measurements for each barrel module are shown in Fig. 18. These distributions showing the overall energy measurement resolution throughout each module are fitted with a simple Gaussian form starting from  $-1.5\sigma$  off the mean values.

The corresponding overall resolutions are 0.93 %, 0.85 % and 0.96 % for the modules P13, P15 and M10 respectively. The main components of these resolutions are: (i) the non-uniformity of the modules, (ii) the local constant terms, (iii) the stochastic terms and (iv) the electronic noise.

The stochastic term (iii) has been precisely measured in [21] at one fixed point and more broadly estimated over the full range in pseudo rapidity in [6]. Taking into account the  $\eta$ -dependence of the stochastic<sup>16</sup> term as derived from [6], the noise as evaluated from random trigger events, the local resolutions and the beam energy spread amounting to 0.08 % a local constant term can be derived for each cell. The distribution of local constant terms yields an average of 0.30 %, 0.25 % and 0.36 % for the P13, P15 and M10 modules respectively. The dispersion of the local constant term is typically of 0.11 % absolute. The overall constant term for all modules can be derived from the average local constant terms by simply adding the measured non-uniformities. The global constant terms obtained are thus 0.52 %, 0.48 % and 0.60 % for the modules P13, P15 and M10, respectively. These results are derived under the assumption that the stochastic term is the same in all modules. A slight variation in the stochastic term could also explain the differences observed between the P13 and P15 resolutions.

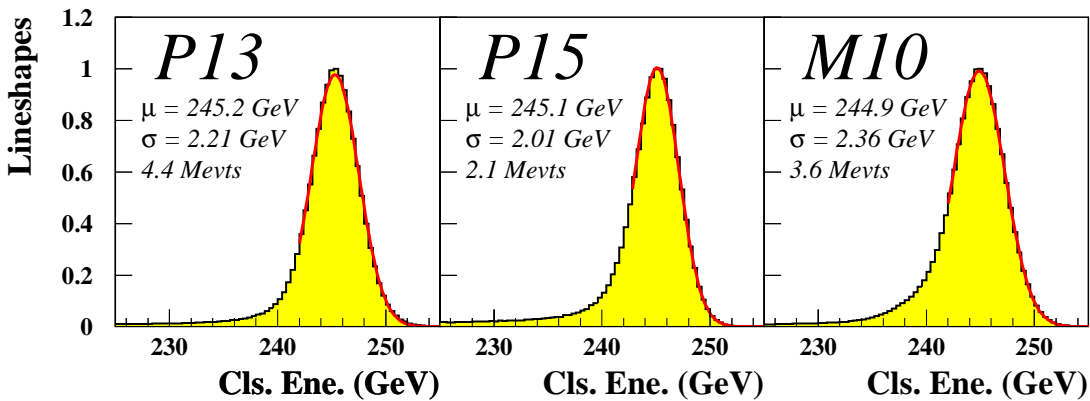


Fig. 18. The energy lineshapes for the barrel modules P13, P15 and M10 containing respectively 4.4, 2.1 and 3.6 million events. The simple gaussian fits to energy peak are displayed and the fit parameters are indicated.

The constant terms (average local or global) are considerably better for the module P15 with respect to the other modules. This observation supports the hypothesis that the module P15 was better manufactured, but could also be due a better stochastic term. All results are summarized in Table 16.

<sup>16</sup> The  $\phi$ -dependence of the stochastic term is assumed to be negligible here.

		Barrel modules		
Module		P13	P15	M10
$< E >$		245.1 GeV	245.0 GeV	244.8 GeV
<b>RMS/<math>&lt; E &gt;</math></b>		<b>0.43 %</b>	<b>0.40 %</b>	<b>0.48 %</b>
$\sigma/\mu$		0.82 %	0.79 %	0.78 %
<b>Local Constant Term</b>		<b>0.30 %</b>	<b>0.25 %</b>	<b>0.36 %</b>
<b>Global Constant Term</b>		<b>0.52 %</b>	<b>0.47 %</b>	<b>0.60 %</b>

Table 9. *Mean energy, non-uniformity, average energy resolution and global constant term for the three tested barrel modules over the entire analysis region.*

## 5 ENDCAP UNIFORMITY

### 5.1 Energy Reconstruction

#### 5.1.1 Clustering Scheme

The electron energy is reconstructed as in the barrel by summing the calibrated energies deposited in the three calorimeter compartments around the cell with the largest energy deposit in the middle compartment. The choices of cluster sizes result from the best compromise between noise and energy leakage. Table 10 summarizes the cluster size in the three compartments. It can be noted that the cluster size changes dramatically in the front compartment due to the variations in the cell granularity. As was the case in the barrel electron clusters the choice of one or two strip cells in  $\phi$  relies upon whether the shower develops near the cell center or not.

	Outer wheel				Inner wheel
$\eta$ -range	[1.5, 1.8]	[1.8, 2.0]	[2.0, 2.4]	[2.4, 2.5]	[2.5, 3.2]
Front	$23 \times 1(2)$	$15 \times 1(2)$	$11 \times 1(2)$	$3 \times 1(2)$	—
Middle	$5 \times 5$				$3 \times 3$
Back	$3 \times 5$				$3 \times 3$

Table 10. *Cluster size ( $\Delta\eta_{cell} \times \Delta\phi_{cell}$ ) per layer around cell with maximum energy deposit.*

### 5.1.2 Reconstruction Scheme

As mentioned in Sec. 3, the barrel and endcap modules were tested in different beam lines at two different maximum energies namely 245 GeV and 119 GeV respectively. At this lower beam electron energy the relative impact of the longitudinal leakage is extremely small but the effect of inactive material is larger. Another major difference intrinsic to the detector is the absence of a presampler. However, the material upstream of the calorimeter is approximately constant. For these reasons the energy reconstruction scheme can be considerably simplified at first order in the endcaps with respect to that used in the barrel. A single normalization factor for all modules can thus be used to derive the total energy from the visible energy measured in the liquid argon. It is derived after all corrections are applied.

Nevertheless two main complications arise: the first one from the continuous decrease of the liquid argon gap with pseudo rapidity (since the HV is set on a sector basis, the signal response will vary with  $\eta$ ); the second from the effective variations of the cluster size with the pseudo rapidity. The fraction of the total 119 GeV electron energy contained in the cluster exceeds 92 % at high  $\eta$  and even more at low  $\eta$ . A single *ad hoc* correction can be derived from the data to correct for both effects simultaneously. This correction is described in Sec. 5.2.1

## 5.2 Cell Level Corrections

### 5.2.1 Ad hoc Residual High Voltage and Leakage Correction

The fact that the liquid argon gap thickness decreases continuously along  $\eta$  whereas the high voltage changes by steps translates into a linear increase in signal response with  $\eta$ , within each high voltage sector. The transverse leakage will affect the energy in an opposite manner and *a priori* not completely linearly, however its effect is expected to be smaller. The overall variation is illustrated in Fig. 19, where the seven (two) HV sectors of the outer (inner) wheel are separated with vertical dashed lines. A good agreement is achieved with a full Monte Carlo GEANT simulation<sup>17</sup> [32]. The crack between the two wheels around  $\eta = 2.5$  distorts the expected linear behavior in sectors B6 and B7. At this level, the non-uniformity of the response over the analysis region (RMS of the mean energy distribution) is around 4 %.

These effects are corrected for by weighting the energy of each cell, depending on its  $\eta$ -position (taken at its center) and its HV sector ( $l$ ), by :

---

<sup>17</sup> The 2 % discrepancy observed in B4 sector is not understood but could be due to a bad tuning of the HV value of  $\sim 50$  V / 1500 V.

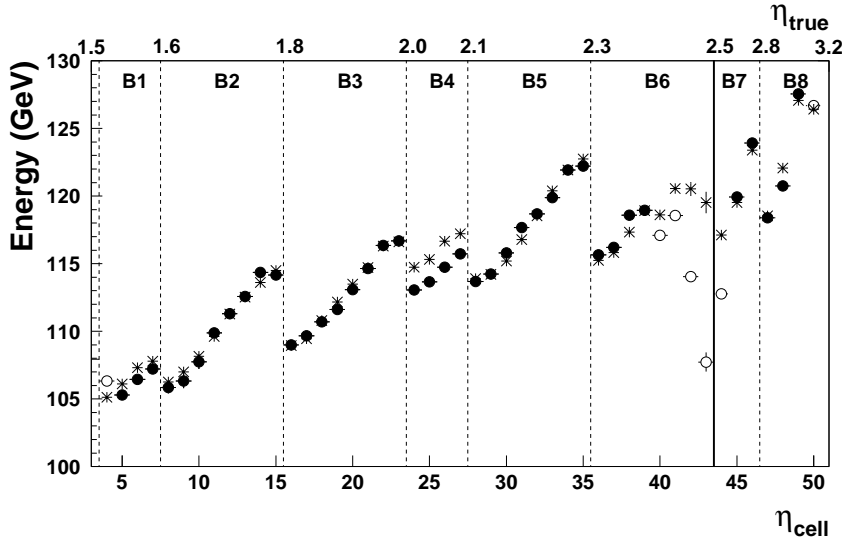


Fig. 19. Energy averaged over  $\phi$  for one module as a function of  $\eta$  before high voltage correction. The vertical dashed lines separate the high voltage sectors and the full line at  $\eta = 2.5$  separates the outer and the inner wheel. The full (empty) dots correspond to cells inside (outside) the analysis region. The stars correspond to the full Monte Carlo simulation results.

$$E_{HV\text{-corr.}}^{\text{cell}}(\eta, l) = E^{\text{cell}} \cdot \frac{\beta^l}{1 + \alpha^l \cdot (\eta - \eta_{\text{center}}^l)} \quad (7)$$

where  $\eta_{\text{center}}^l$  is the  $\eta$ -value at the center of HV sector  $l$ . The coefficients  $\alpha^l$  and  $\beta^l$  are the correction parameters of sector  $l$ ,  $\beta^l$  being a normalization factor, close to 1, accounting also for inaccurate high voltage settings. They are determined by a linear fit. The inner wheel case is more complicated and the resulting parameters are slightly biased. The results obtained for  $\alpha^l$  and  $\beta^l$  in the eight scanned HV sectors<sup>18</sup> are shown in Fig. 20 for the three tested modules.

A good agreement between modules is observed and  $\alpha$  depends very weakly on  $\eta$ . Therefore a single value of  $\alpha = 0.49$ , in good agreement with the full Monte Carlo simulation, is used for all modules.

### 5.2.2 Capacitance correction

Along the  $\phi$  direction, the gap thickness is in principle kept constant by the honeycomb spacers. However, the energies measured in the test beam show an unexpected non-uniformity along  $\phi$ , almost at the percent level [34,35]. This effect can be correlated with the variations of middle cell capacitance along  $\phi$  measured independently, as shown in Fig. 21 for ECC0. The  $\phi$ -dependence of

<sup>18</sup> The first HV sector, covering the  $\eta$ -range [1.375-1.5], has not been completely scanned (at most 2 cells in  $\eta$ ) and is not included in the analysis.

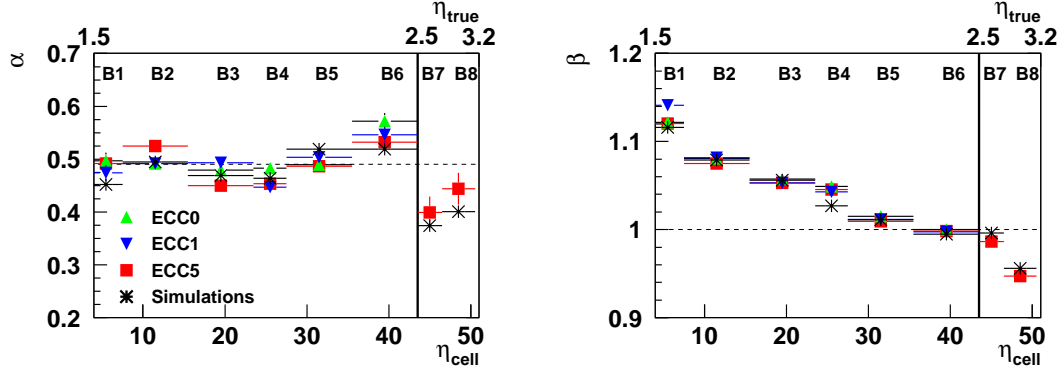


Fig. 20. High voltage correction parameters  $\alpha$  (left) and  $\beta$  (right) obtained in the eight scanned HV sectors for the three tested modules. Results have been averaged over  $\phi$ . The vertical full line at  $\eta = 2.5$  separates the outer and the inner wheel. The stars correspond to the full Monte Carlo simulation results.

the energy can thus be explained by local fluctuations of the gap thickness, generated during the module stacking. The effect is almost independent of  $\eta$ . Even if it corresponds to small absolute deviations (the gap thickness is roughly 3 mm at low  $\eta$  and 1 mm at high  $\eta$ , 1 % represents only a few tens of microns), it must be corrected in order to achieve the best response uniformity.

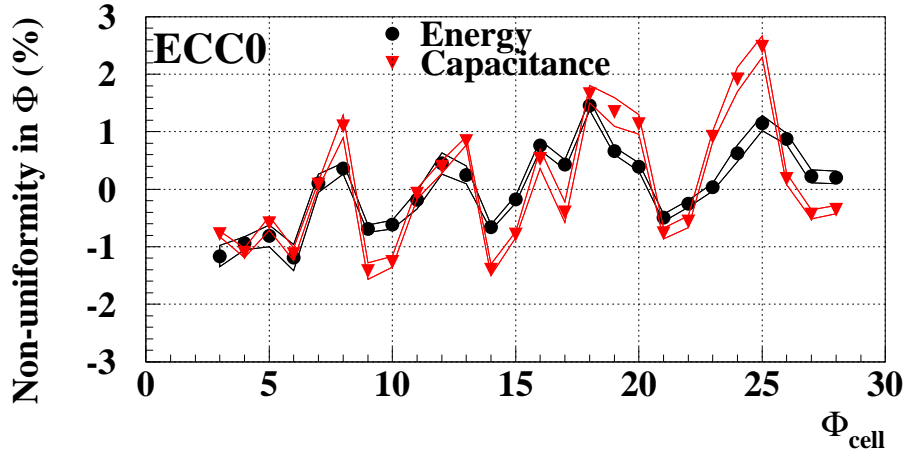


Fig. 21. Variation along the  $\phi$  direction of the measured ECC0 outer wheel middle cell capacitance (red triangles) and of the energy measured in beam test (black points). All points have been averaged over  $\eta$ .

The energy is then corrected by weighing each cell in the following way :

$$E_{capa-corr.}^{cell}(\phi) = E^{cell} / \left( \frac{C_\phi}{\langle C_\phi \rangle} \right)^\alpha \quad (8)$$

where  $C_\phi$  is the cell capacitance,  $\langle C_\phi \rangle$  is its average over all  $\phi$  and  $\alpha$  the high voltage correction parameter (see section 5.2.1). The effect is assumed to be independent of the depth. The middle cell measurements are used for

all compartments. The  $\alpha$  exponent was empirically chosen but was found to yield a near to optimal uniformity. It illustrates the interplay between the high voltage and the capacitance corrections. Such a correction is not performed in the ECC5 inner wheel, whose uniformity along  $\phi$  is very good. For ECC1, no accurate capacitance measurement was made. An *ad hoc* correction is thus extracted from the  $\phi$ -dependence of the energy averaged over  $\eta$ . As it corrects for local stacking effects, the correction has to be specific for each cell and each module. In ATLAS the correction based on the capacitance measurements could be further refined by inter calibrating  $\phi$ -slices of the calorimeter with  $Z^0 \rightarrow e^+e^-$  events.

### 5.3 Cluster Level Corrections

#### 5.3.1 Cluster Energy Correction for High Voltage problems

Another problem, which appeared on ECC1, was that two electrode sides, which were on spare lines, were not holding the high voltage, inducing an energy loss depending on the event impact point position in  $\phi$  with respect to the faulty electrode. The dependence of the cluster energy with  $\phi$  was parametrized and corrected with a parabola. The energy resolution of the affected cells is degraded by  $\sim 50\%$  and the uniformity in the corresponding HV zone ( $\Delta\eta \times \Delta\phi \sim 0.2 \times 0.4$ ) is degraded by  $\sim 20\%$ .

#### 5.3.2 Endcap $\eta$ and $\phi$ energy modulation corrections

To correct for energy variations along the  $\eta$  direction a parametrization similar to that used in the barrel is considered. However, as the transverse size of the electromagnetic shower is constant and the cell dimension decreases with pseudo rapidity, the leakage is expected to increase with  $\eta$ , and thus the absolute value of the quadratic term of the parabola is expected to increase with pseudo rapidity. This effect is sizable only in EC modules and a good agreement is achieved among the three tested modules. The quadratic parameter is linearly parametrized as a function of  $\eta$  [34].

The  $\phi$  modulation for EC modules is fitted and corrected for with the following function [36] :

$$E_{\phi\text{-corr.}}(\phi_{abs}) = E / \left( 1 + \sum_{i=1}^2 a_i \cos [2\pi i(\phi_{abs} - \Delta\phi)] + b_1 \sin [2\pi\phi_{abs}] \right) \quad (9)$$

where  $\phi_{abs}$  is in absorber units,  $a_1$  and  $a_2$  are the coefficients of the even

component (it has been checked that only two terms are necessary),  $b_1$  the coefficient of the odd component one and  $\Delta\phi$  a phase shift. The parameters of the fits are displayed in Fig. 22 for all three endcap modules. A good agreement between the fitted parameters for the different modules is observed. Given the non trivial geometry of the endcap modules this result highlights the manufacturing quality of the modules. As was the case for the barrel modules, a single correction derived from a fit of the coefficients can be used.

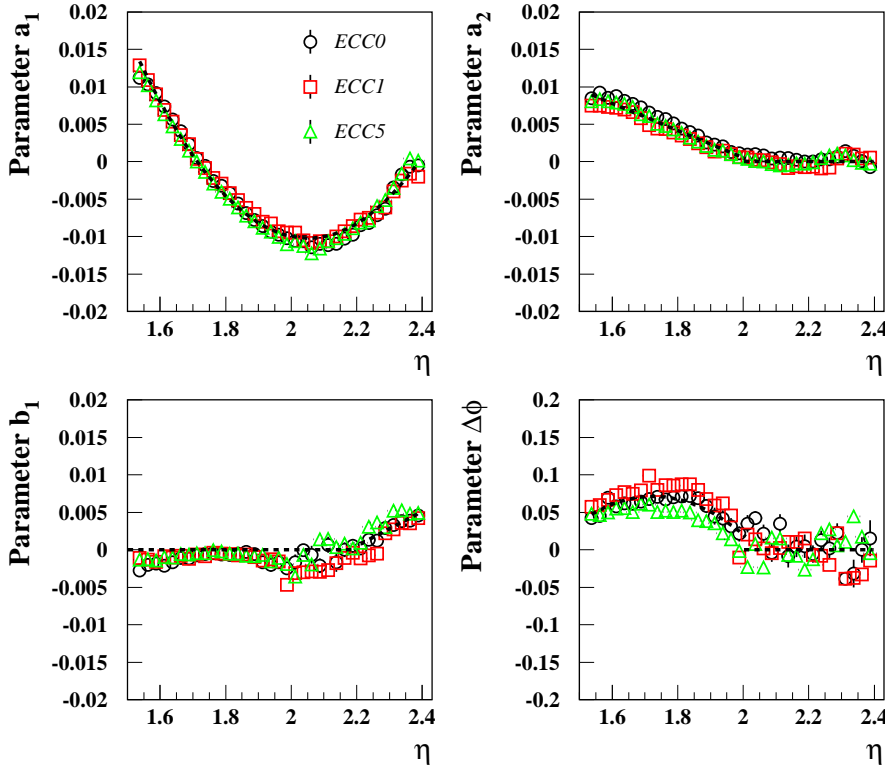


Fig. 22. Coefficients of  $\phi$ -modulation corrections, averaged over  $\phi$ , as a function of  $\eta$  for the three tested modules. Their linear or parabolic parametrisations are superimposed.

#### 5.4 Modules uniformity

The mean energies as reconstructed from a gaussian fit to the energy distribution after all corrections are shown in Fig. 23 for all the cells and for the three tested modules. Their dispersion across the outer wheel analysis region is approximately 0.6 % for all modules [34]. It is better for ECC1 because an *ad hoc* capacitance correction was used. A similar result is obtained for the ECC5 inner wheel: the response non-uniformity over the 25 cells is approxi-

mately 0.6 %.

With the high voltage correction the uniformity is of the order of 1 % (0.78 % for ECC0, 0.86 % for ECC1 and 0.65 % for ECC5). The capacitance correction yields an uniformity close to final one. Cluster level corrections do not significantly impact the module response uniformity, but they improve the energy resolutions. The problematic channels (for instance for high voltage failures in ECC1 and ECC5), that have been kept, do not degrade the results. If they were excluded, the non-uniformity would improve by less than 0.01 %. These results are summarized in Table 11.

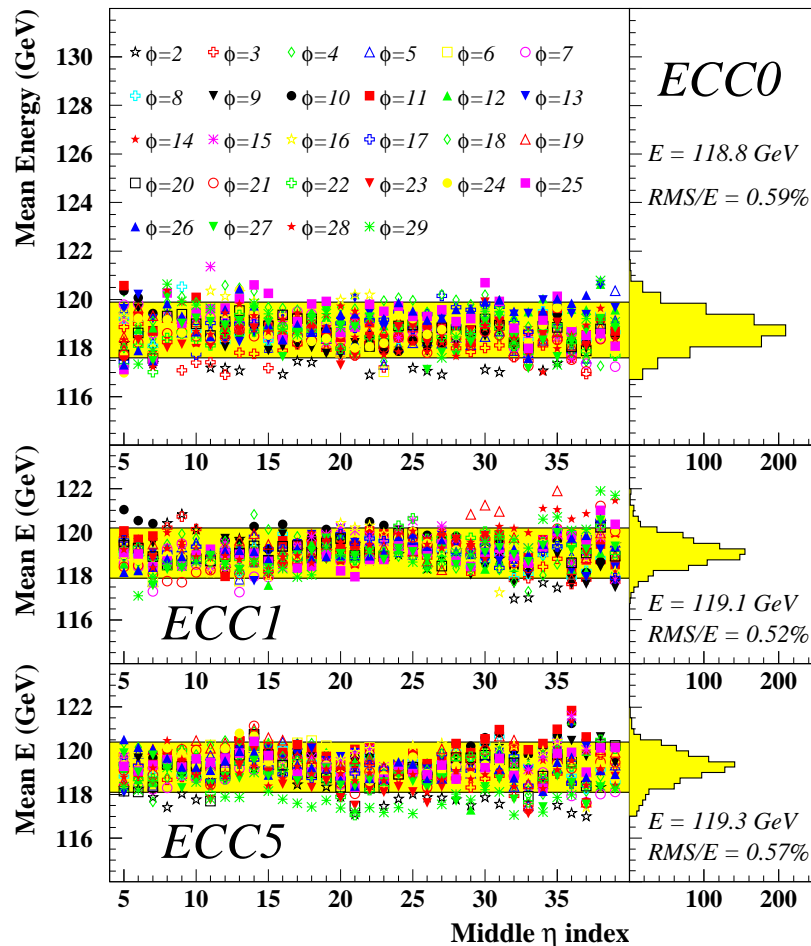


Fig. 23. Mean reconstructed energy as a function of the hit cell position in  $\eta$  for a 119 GeV electron beam. Results are shown for the outer wheel of all three tested modules.

## 5.5 Resolution and Overall Constant Term

The energy resolution as derived from the fit to the energy distribution for all cells and after all corrections are applied is shown in Fig. 24. When quadratically subtracting the electronic noise term of  $\sim 200$  MeV and a beam spread of 0.07 % the energy resolutions are compatible with those reported in [7]. Assuming an average local constant term of 0.35 % an average value of the stochastic term of  $11.4 \pm 0.3$  %/ $\sqrt{E}$  is found.

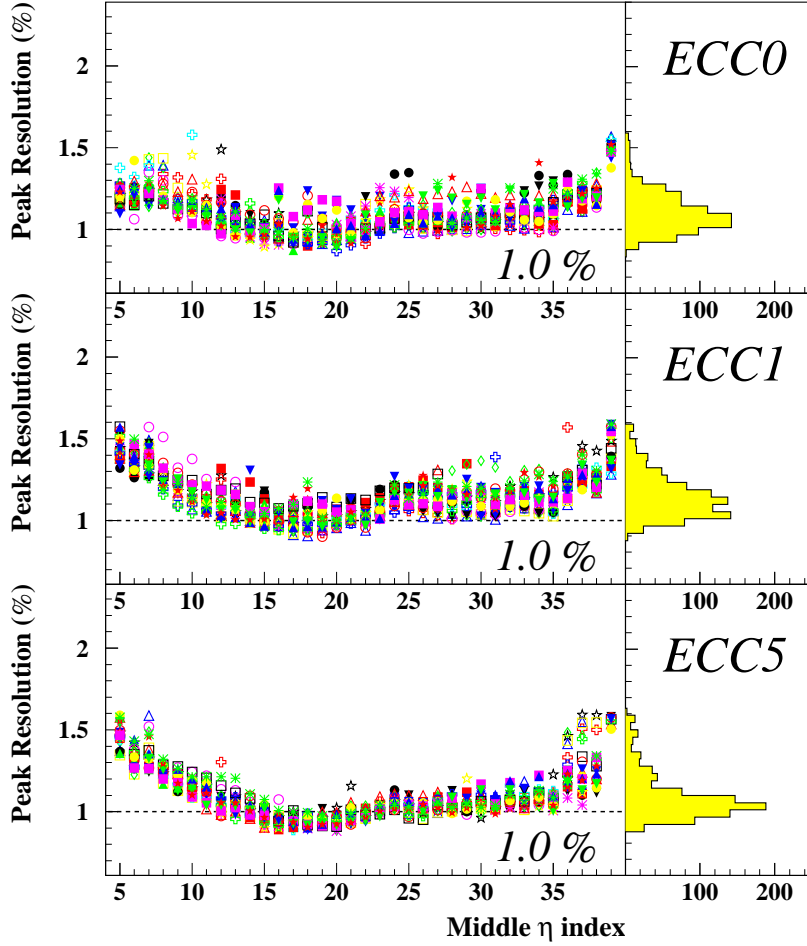


Fig. 24. Reconstructed energy resolutions as a function of the hit cell position in  $\eta$  for a 119 GeV electron beam. Results are shown for the three tested modules (outer wheel). The legend used for the different  $\phi$  values here is the same as in Fig. 23

The overall constant term of the energy resolution is estimated from the cumulative energy distribution of all cells of the analysis domain. These energy lineshapes are illustrated in Fig. 25 for all tested modules. Each of these en-

Module	Outer wheel			Inner wheel
	ECC0	ECC1	ECC5	ECC5
$\langle E \rangle$	118.8 GeV	119.1 GeV	119.3 GeV	119.1 GeV
<b>RMS/<math>\langle E \rangle</math></b>	<b>0.59 %</b>	<b>0.52 %</b>	<b>0.57 %</b>	<b>0.60 %</b>
$\sigma/\mu$	1.27 %	1.28 %	1.22 %	1.26 %
<b>Constant Term</b>	<b>0.70 %</b>	<b>0.72 %</b>	<b>0.61 %</b>	<b>0.78 %</b>

Table 11. *Mean energy and non-uniformity of the three tested modules over the whole analysis region. For the outer (inner) wheel, statistical errors on the mean energy are  $\sim 0.02$  GeV (0.1 GeV) and statistical errors on non-uniformity are  $\sim 0.02$  % (0.1 %).*

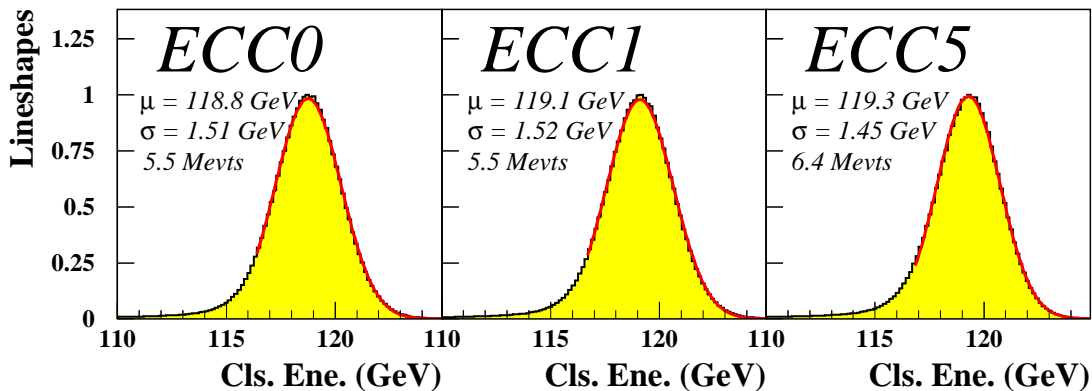


Fig. 25. *The energy lineshapes for the endcap modules ECC0, ECC1 and ECC5 containing respectively 5.5, 5.5 and 6.4 million events. The simple gaussian fits to energy peak are displayed and the fit parameters are indicated.*

ergy spectra is fitted with a simple Gaussian form starting from  $-1.5\sigma$  off the mean value. When unfolding a sampling term of  $\sim 11.4 \pm 0.3$  GeV $^{1/2}$  an electronic noise term of  $\sim 200$  MeV and the beam spread contribution amounting to  $\sim 0.07$  % an overall constant term of  $\sim 0.7$  % is found. The global constant terms for all endcap modules are reported in Table 11.

## CONCLUSION

The response uniformity of the ATLAS liquid argon electromagnetic calorimeter to high energy electrons has been studied in the pseudo rapidity range

from 0 to 3.2. These results encompass both the barrel and endcap calorimeters which were independently tested in different beam lines using 245 and 119 GeV electrons respectively. The uniformity in the pseudo rapidity range from 0 to 2.4 is illustrated in Fig. 26.

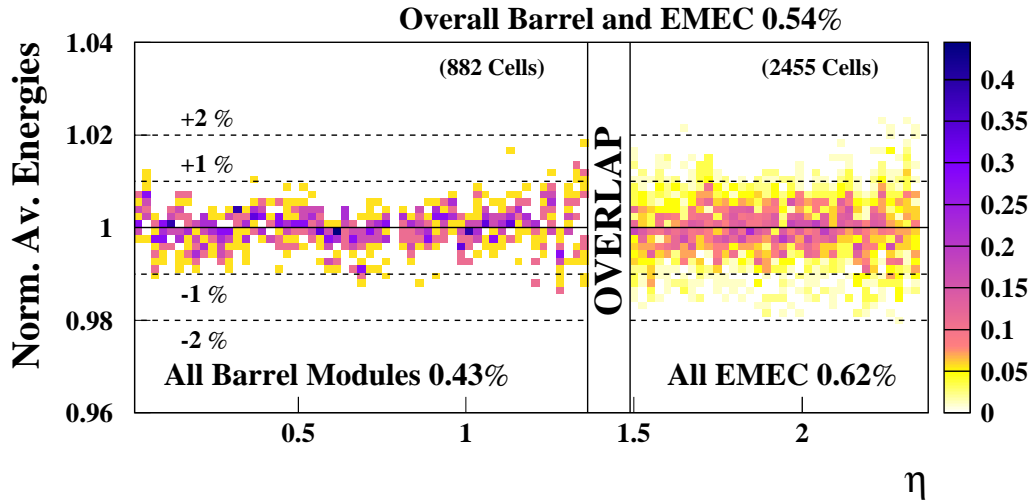


Fig. 26. Two dimensional histogram of the average energies measured in all cells of all tested modules normalized to the mean energy of the modules. In the barrel the energies were  $\sim 245$  GeV and  $\sim 120$  GeV in the EMEC. The distributions are normalized to the number of middle cells scanned in  $\phi$  for each value of  $\eta$ .

For the barrel modules a modified version of the energy reconstruction scheme developped in [21] mostly based on a full Monte Carlo simulation is used. Most potential sources of non-uniformity were reviewed and their impact was independently estimated. When comparing the estimated non-uniformity to the measured one a very good agreement is observed thus indicating that the sources of non-uniformity are well understood. For the endcap modules the material upstream of the calorimeter is approximately constant, a simpler energy reconstruction scheme is thus applied. A full Monte Carlo simulation accounting for the complex geometry of EMEC modules is performed and is in good agreement with the data.

Non uniformities of the response do not exceed 7 %. Overall constant terms in the energy resolution are derived and range between 5 % and 7 %. Such performance is within the calorimeter design expectations.

## ACKNOWLEDGMENTS

We would like to thank the accelerator division for the good working conditions in the H8 and H6 beam lines. We are indebted to our technicians for their contribution to the construction and running of all modules. Those of us from non-member states wish to thank CERN for its hospitality.

## References

- [1] B. Aubert *et al.* (RD3 Collaboration), *Nucl. Instrum. Meth. A* **309**, 438 (1991).
- [2] B. Aubert *et al.* (RD3 Collaboration), *Nucl. Instrum. Meth. A* **321**, 467 (1992).
- [3] B. Aubert *et al.* (RD3 Collaboration), *Nucl. Instrum. Meth. A* **325**, 118 (1993).
- [4] D. M. Gingrich *et al.* (RD3 Collaboration), *Nucl. Instrum. Meth. A* **364**, 290 (1995).
- [5] D. M. Gingrich *et al.* (RD3 Collaboration), *Nucl. Instrum. Meth. A* **389**, 398 (1997).
- [6] B. Aubert *et al.* (The ATLAS Electromagnetic Liquid argon Calorimeter Group), *Nucl. Instrum. Meth. A* **500**, 202 (2003).
- [7] B. Aubert *et al.* (The ATLAS Electromagnetic Liquid argon Calorimeter Group), *Nucl. Instrum. Meth. A* **500**, 178 (2003).
- [8] ATLAS Collaboration, Liquid Argon Calorimeter Technical Design Report, CERN-LHCC/96-41.
- [9] B. Aubert *et al.*, ATLAS Electromagnetic Liquid Argon Calorimeter group *Nucl. Instrum. Methods A* **558** (2006) 388.
- [10] B. Aubert *et al.*, ATLAS Electromagnetic Liquid Argon Calorimeter group *Nucl. Instrum. Methods A* **539** (2005) 558.
- [11] M. L. Andrieux *et al.*, *Nucl. Instrum. Methods A* **479** (2002) 316.
- [12] J. Colas *et al.*, ATLAS Note ATL-LARG-2000-004.
- [13] P. Pralavorio and D. Sauvage, ATLAS Note ATL-LARG-2001-006.
- [14] F. Berny *et al.*, ATLAS Note ATL-LARG-2003-005.
- [15] G. Garcia *et al.*, *Nucl. Instrum. Meth. A* **418**, 513 (1998).
- [16] P. Barrillon *et al.*, ATLAS Note ATL-LARG-2003-004.
- [17] S. Baffioni *et al.*, ATLAS Note ATL-LARG-PUB-2007-005.
- [18] J. Colas *et al.* ATLAS Note ATL-LARG-2000-006, 2000.

- [19] W. Willis and V. Radeka. Nucl. Instrum. Meth. A **120** (1974).
- [20] W.E. Cleland and E.G. Stern. Nucl. Instrum. Meth. A **338** (1984).
- [21] M. Aharrouche *et al.*, Nucl. Instrum. Meth. A **568**, 601 (2006).
- [22] M. Lefebvre, G. Parrou and P. Petroff, RD3 internal note 41, 1993.
- [23] M. Citterio, M. Delmastro and M. Fanti, ATLAS Note ATL-LARG-2001-018, 2001.
- [24] L. Neukermans, P. Perrodo and R. Zitoun, ATLAS Note ATL-LARG-2001-008, 2001.
- [25] D. Banfi, M. Delmastro and M. Fanti. *Journal of Instrumentation*, 1:P08001, 2006.
- [26] D. Prieur. ATLAS Note ATL-LARG-2005-001, 2005.
- [27] C. De La Taille, L. Serin, ATLAS Note ATL-LARG-1995-029, 1995.
- [28] W. Walkowiak, ATLAS Note ATL-LARG-99-009, 1999.
- [29] F. Hubaut, B. Laforge, D. Lacour, F. Orsini, ATLAS Note ATL-LARG-2000-007, 2000.
- [30] F. Hubaut, ATLAS Note ATL-LARG-2000-009.
- [31] B. Dekhissi, J. Derkaoui, A. El-Kharrim, F. Hubaut, F. Maaroufi and P. Pralavorio, ATLAS Note ATL-LARG-2003-012.
- [32] S. Agostinelli *et al.* (GEANT4 Collaboration), Nucl. Instrum. Meth. A **506**, 250 (2003).
- [33] G. Graziani, ATLAS Note ATL-LARG-2004-001.
- [34] F. Hubaut and C. Serfon, ATLAS Note ATL-LARG-2004-015.
- [35] S. Rodier, PhD Thesis CERN-THESIS-2004-001 (2003).
- [36] G. Garcia, PhD Thesis DESY-THESIS-2000-010 (2000).